REVISION 3

The Structure of Water-Saturated Carbonate Melts

Dionysis I. Foustoukos and Bjorn O. Mysen

Geophysical Laboratory, Carnegie Institution of Washington, 5251 Broad Branch Rd. NW, Washington DC 20015

Keywords: carbonate melt, water, melting-point depression, trace elements, hydrothermal diamond anvil cell, Raman vibrational spectroscopy

ABSTRACT

The structure of water-saturated Ca- and Mg-bearing carbonate melts under reducing and oxidizing conditions was investigated in a series of hydrothermal anvil cell experiments conducted at 400 - 1100 ^{o}C and 442 – 2839 MPa. Equilibria were investigated in the calcite-H_2O, calcite-CaO-H_2O, magnesite-H_2O and magnesite-MgO-H_2O systems, with redox conditions controlled by Re/ReO_2 and Ti/TiO_2 assemblages. Melting relationships and the C-O-H speciation of the coexisting aqueous fluid and melt were assessed *in-situ* by Raman vibrational spectroscopy. Hydrous melting of $MgCO_3$-MgO occurred at ~ 850 ^{o}C, 1.5-2 GPa. In the $CaCO_3$-CaO-H_2O system, melt was formed at 600 - 900 ^{o}C and pressures of 0.5 – 1.5 GPa because of melting-point depression imposed by the presence of CaO. The C-O-H speciation of the carbonate melts and coexisting supercritical aqueous solutions was mainly H_2O and CO_3^{2-}, with traces of $CO_{2(aq)}$ and $CH_{4(aq)}$ in the fluid phase. The melt-fluid H_2O partition coefficients attained in the Mg-bearing melt (median 0.5) were higher than in the Ca-bearing melt (median 0.3). Under oxidizing redox conditions, dissolved ReO_2^- was present in all phases, underscoring the enhanced solubility of metals in carbonate-bearing melts and

carbonatites. In effect, the enhanced solubility of H_2O along with the ionic nature of the carbonate melts may promote the solvation of ionic species in the melt structure.

From *in-situ* vibrational spectroscopy, the v_1-CO_3^{2-} vibration recorded in the melt spectra suggests the presence of intermolecular interactions between the oxygen of the carbonate ion with water dissolved in the melt. The thermodynamic properties of this water appear to be similar to the supercritical aqueous phase. For example, the estimated enthalpy for the breakage of the hydrogen bonding between water molecules attained values of 6.8 ± 1.5 kcal/mol and 8.4 ± 1.3 kcal/mol in the melt and fluid phase, respectively. The calculated partial molar volume of H_2O in the melt (~ 48 ± 6 cm^3/mol) is also comparable to the partial molar volume of supercritical water at similar conditions. Interestingly, this value is considerably greater than published partial molar volume values for H_2O in silicate melts (10-12 cm^3/mol).

The pressure-temperature melting relationships of the CaO-CO_2-H_2O and MgO-CO_2-H_2O systems highlight the important role of water and alkaline earth oxides on the hydrous melting of the carbonate-bearing subducting oceanic crust. Carbonates present in marine sediments or serpentinized peridotites may melt before complete dehydration at the slab-mantle wedge transition zone, and thus, never reach sub-arc depths. To this end, melting of carbonate minerals at crustal temperatures and pressure can contribute to the volcanic CO_2 flux at the arc through melt/fluid interactions.

INTRODUCTION

Carbonatites, igneous rocks derived from carbonate melts (Streckeisen, 1980), are thought to be originated from small degree melts in the asthenospheric mantle (e.g. (Gudfinnsson and Presnall, 2005; Nelson et al., 1988)), although a lithospheric origin (Bell and Blenkinsop, 1989) and more complex models of refertilization and melting may be operational (Bizimis et al., 2003). Recent studies also suggest origins as deep as the mantle transition zone (Dalou et al., 2009). Understanding the structure of carbonate melts is important towards constraining the cycling of C-O-H-N volatiles and trace element/metal mobility in the Earth's interior (Jones et al., 2013).

Experimentally, phase equilibrium relationships in the CaO-CO_2-H_2O and MgO-CO_2-H_2O systems have been extensively studied over a wide range of pressure, temperature conditions and for varying water content, in order to address melting behavior of calcite and magnesite coexisting with Ca-Mg oxides and hydroxides (Boettcher et al., 1980; Irving and Wyllie, 1975; Walter et al., 1962; Wyllie and Boettcher, 1969; Wyllie and Tuttle, 1959; Wyllie and Tuttle, 1960). Overall, it's commonly concluded that hydrous melting of calcite-lime and magnesite-periclase assemblages commences at significantly lower temperatures (<900 ^{o}C) than for the pure carbonate-fluid equilibria (>1200 ^{o}C) at upper mantle pressure conditions (Walter et al., 1962; Wyllie and Tuttle, 1960).

Water solubility in carbonate melts is significantly higher than in alkaline silicate melts, reaching values of nearly of 15 wt % at 100 MPa, 900 ^{o}C (Keppler, 2003), whereas in silicate melts the solubility is only several wt % under such temperature and pressure conditions (e.g., (Holtz et al., 1995)). This high water content likely enhances the

solubility of metal cations (Veksler and Keppler, 2000), and, along with the ionic (Zarzycki, 1961) and likely alkaline nature of molten carbonates, may be the reason for the elevated concentrations of REE and other incompatible trace elements in carbonatites (Veksler et al., 2012). However, the ionic behavior of structural CO_3^{2-} and the distribution of hydroxyl/molecular H_2O in carbonate melts are poorly understood, mainly because these phases cannot be quenched to ambient conditions (Genge et al., 1995). The very limited data that exist are from experimental studies involving diamond anvil cell techniques (Chou et al., 1995; Williams and Knittle, 2003).

Here, we present a series of hydrothermal diamond anvil experiments conducted at 400 – 1100 ^{o}C and 442 – 2839 MPa where calcite/CaO- and magnesite/MgO- derived melts coexisted with aqueous solutions under reducing and oxidizing conditions. Raman vibrational spectroscopy was employed to monitor C-O-H speciation in both the melt and fluid phase *in-situ*, and to describe the intermolecular interactions between ionic (e.g. CO_3^{2-}, Ca^{2+}, Mg^{2+}) and neutral species (e.g. H_2O). The experimental data are combined with existing measurements of water solubility in Ca-Na-Mg carbonate melts at lower pressure (Keppler, 2003) to assess the thermodynamic properties of H_2O in the structure of carbonate melts and to estimate partition coefficients between melt and fluid.

EXPERIMENTAL SECTION

Experiments were performed by utilizing externally-heated hydrothermal diamond anvil cells (HDAC) equipped with low fluorescence 1-mm culet diamonds (Bassett et al., 1996). The sample chamber (500 μm I.D.) was structured between the anvil faces in a 125 μm thick rhenium gasket. Temperature was monitored with chromel-

92 alumel thermocouples in contact with the upper and lower diamonds. Pressure was
93 derived by measuring the temperature/-pressure dependent Raman frequency shift of
94 synthetic ^{13}C diamond (Schiferl et al., 1997), with an uncertainty of about ± 40 MPa
95 (Mysen and Yamashita, 2010) that corresponds to a ± 0.1 cm^{-1} frequency uncertainty on
96 the fundamental band of the ^{13}C diamond. This level of accuracy is achieved by
97 performing acquisitions at 2400 grooves/mm of the holographic gratings in our JASCO
98 NRS-3100 microRaman systems and then normalizing the Raman shift to the 584.72 nm
99 Ne emission line. The Ne emission line and the Raman shift of the ^{13}C-diamond
100 stretching band are recorded on the same spectroscopic window with a 532 nm
101 continuous wave laser line (see below). To this end, the Ne emission line is used as
102 internal standard for the position of the spectrophotometer at each acquisition of ^{13}C-
103 diamond spectra (Schiferl et al., 1997). The methodology adopted has been calibrated in
104 HDAC experiments involving pure H_2O by using the equation of state of pure H_2O to
105 constrain the *in-situ* pressure at measured temperature (Mysen and Yamashita, 2010).
106 An experimental design was employed, which uses direct-sintered silicon carbide
107 for the diamond seat assembly. This material (UltraSIC, SC-30, Coorstek) exhibits
108 substantially greater hardness (26 GPa) and thermal conductivity (150 W/m K) than the
109 commonly-used tungsten carbide, while sustaining maximum operational temperatures of
110 nearly 1600 ^oC[1]. The SC-30 diamond seats allow HDAC experiments to be conducted to
111 temperatures of 1500 ^oC, and pressure > 3 GPa. Molybdenum wire was placed around the
112 silicon carbide seats to heat the entire sample chamber (±1 ^oC accuracy).

[1] http://www.coorstek.com/resource-library/library/8510-1364_ceramic_properties_mp.pdf

Raman Spectroscopy Instrumentation: Vibrational spectroscopy data were collected with a Jasco model NRS-3100 confocal microRaman spectrometer equipped with a λ_{ex} = 532 nm continuous wave laser line (~7 mW at the sample). The beam diameter was nearly 1 μm with a 10 μm focal depth. Signal detection was through 50X/0.42 numerical aperture (N.A.) long-working distance Mitutoyo™ objective lenses. Raman signal was dispersed using 600, 1200 and 2400 grooves/mm. The spectral window was centered at 1100 cm^{-1}, 1250 cm^{-1}, 2250 cm^{-1}, 2400 cm^{-1}, 2800 cm^{-1} and 3600 cm^{-1} with a frequency resolution of 1-2 cm^{-1} at 2400 grooves/mm. The signal was collected with a Peltier-cooled CCD (Andor™ Model DV401-F1 1024x128 pixel with 25 μm pixel size). Acquisition time ranged from 100 to 400 sec/CCD window depending on the signal intensity of the sample. Two acquisitions per window were collected.

Curve-fitting of the Raman spectra was performed using the commercial software Igor from Wavemetrics™. Background subtraction was conducted by fitting a third-order polynomial function through portions of the spectra with baseline signal intensity only. Replicate measurements were acquired at the same beam spot and with the same instrumental parameters to constrain uncertainties on spectra analysis and processing. The standard deviation on the integrated areas between the fitted Raman spectra in each acquisition reflects a 5% level of uncertainty, which is larger than the uncertainty estimated for the integrated area of each individual Raman peak (Foustoukos and Mysen, 2013).

Experimental Procedures: Experiments were designed to study the evolution of carbonate melts coexisting with a discreet fluid phase at conditions ranging from 400 to 1100 ^{o}C and from 442 MPa to 2839 MPa (Table 1) in the CaO-CO_2-H_2O and MgO-CO_2-

H_2O systems. Experiments were conducted under oxidizing and reducing redox conditions (Table 1) constrained by the presence of Re/ReO_2 and Ti/TiO_2 redox buffers, respectively. This was accomplished by the addition of ReO_2 powder or a titanium metal chip in the sample chamber. These phases (e.g. Ti, TiO_2) were identified in the quenched reaction products. At the experimental conditions of this study, titanium solubility in supercritical fluids should be minimal (Audétat and Keppler, 2005; Tropper and Manning, 2005). However, this appears not be the case for the rhenium species (Xiong and Wood, 1999) (see later in discussion). Raman spectra of C-O-H species dissolved in the aqueous solution and melt phase were recorded at elevated temperature/-pressure conditions, and also in samples quenched to ambient conditions ("*ex-situ*"). Quenching was commenced at a rate of ~600 ^{o}C/min until the temperature reached 100 ^{o}C, and then at 25 ^{o}C /min to room temperature. During quenching, degassing of C-O-H volatiles (H_2, CO_2, CH_4) resulted to the formation of a discreet gas phase ("bubble").

Carbonate reactants were dried at 400 ^{o}C for 72 hours, and the Ca-Mg oxides were fired at 1000 ^{o}C for 3 hours prior to experiments. Dehydrated $CaCO_3$, CaO, $MgCO_3$, and MgO were stored at 300 ^{o}C prior to loading in the HDAC. The sample consisted of mineral mixtures and H_2O at volumetric ratios ~ 2:1 (empirically assessed) resulting to fluid-melt immiscibility at elevated temperatures and pressures (Fig. 1). In addition, ReO_2 powder was allowed to equilibrate with H_2O in a carbonate-free experiment to characterize the speciation of rhenium dissolved in supercritical aqueous solutions, and to accurately identify the frequency position and shape of the stretching fundamental vibrations (ν_1) of dominant Re-bearing aqueous species (Xiong and Wood, 2001; Xiong and Wood, 1999) at high pressures and temperatures (Table 1).

Spectroscopic data of the melt are strictly from samples volumes within melt pockets encapsulated within the entire height of the sample chamber (Fig. 1a). This was accomplished by evaluating the vertical position of the melt globules relative to the surface of both the upper and lower diamond. The carbonate melting experiments were conducted for at least 12 hours. The samples remained at each experimental condition for more than 2 hours. Time series measurements performed *in-situ* at high temperature/-pressure indicate that equilibrium was reached at all conditions, which is consistent with the equilibration reaction times reported in previous studies involving melting relationships in the calcite-lime-H_2O and magnesite-periclase-H_2O system (Chou et al., 1995; Walter et al., 1962; Wyllie and Boettcher, 1969; Wyllie and Tuttle, 1960).

RESULTS AND DISCUSSION

Melting of carbonates under water-saturated conditions

Hydrous melting experiments of the $CaCO_3$-CaO and $MgCO_3$-MgO assemblages were conducted along a pressure and temperature path that follows the oceanic geotherm (Green and Ringwood, 1963a; Green and Ringwood, 1963b). The highest temperature of 1100 ^oC was reached at nearly 3 GPa (Fig. 2a). In some cases, conditions resembled those at the hot subduction zone of Central Cascadia (Syracuse et al., 2010). Experimental conditions attained are relevant to subduction zone environments and within the range of pressures and temperatures that permit hydrous melting of the subducted oceanic crust and lithosphere (Grove et al., 2012; Till et al., 2012).

In-situ experimental observations (Fig. 1) indicate that hydrous melting of the carbonate-oxide assemblages occurred at temperatures lower than 850 ^oC (1 - 2 GPa)

consistent with the melting relationships predicted in previous studies (Fig. 2b). For example, Walter et al. (1962) predicted a five phase (MgO-$MgCO_3$-H_2O-$Mg(OH)_2$-melt) invariant point at conditions greater than 700 ^oC, 400 MPa but less than 1 GPa, whereas Ellis and Wyllie (1979) projected this point to 1210 ^oC, 4.6 GPa. In our experiments, a sharp transition between magnesite-periclase-fluid and melt-fluid equilibria was documented at ~ 850 ^oC, 1.5 – 2 GPa (Fig. 2b). Melting of calcite in the presence of CaO and H_2O appears to occur at temperatures lower than 600 ^oC (0.5 – 1.5 GPa) extending to nearly 900 ^oC (1 – 1.5 GPa), whereas in same occasions melting coincided with calcite in the aqueous fluid phase (i.e. Cc-melt (Cc-CaO)-H_2O system in figure 2b, 1b). Phase equilibria in the ternary CaO-H_2O-CO_2 system formulated by Wyllie and Turtle (1960) also show the three-phase domains of calcite-CaO-melt and calcite-melt-H_2O separated by the fields of calcite-melt and calcite-H_2O at 685 – 920 ^oC and 0.1 GPa. f_{O_2} conditions have been suggested to control the hydrous melting of calcite (Chepurov et al., 2011; Lazar et al., 2014), however, we were not able to observe discreet differences on the melting temperature of systems bearing Re/ReO_2 (oxidizing) or Ti/TiO_2 (reducing) mineral redox buffers.

Our *in-situ* HDAC observations highlight the important role of CaO on imposing a melting-point depression on calcite under water-saturated conditions. Experiments that involved pure calcite coexisting with aqueous phase at 950 ^oC and 1.5 GPa (Table 1) did not produce carbonate melts under these conditions, which is consistent with the well-known extensive stability field of calcite (Fig. 2b) (Wyllie and Boettcher, 1969). Hydrous melting of pure magnesite, however, did occur at temperatures and pressures similar to those attained in the $MgCO_3$-MgO-H_2O experiments (Fig. 2b). Such a relatively low

205 temperature (< 1000 °C), high pressure (> 1 GPa) melting of magnesite has been
206 predicted for conditions of low CO_2 fugacity in a H_2O dominant vapor phase (Ellis and
207 Wyllie, 1979). Even though it is not possible to determine quantitatively the
208 concentration of fluid-dissolved $CO_{2(aq)}$ in the experiments, thermodynamic models
209 suggest that for the calcite/-magnesite-H_2O system the $CO_{2(aq)}$ concentrations should not
210 exceed 0.01 molal at 700-727 °C, 1 GPa (f_{CO_2} ~ 1 (Johnson et al., 1992))(Manning,
211 2013; Pan et al., 2013). Significant lower f_{CO_2} are expected during hydrous melting of
212 carbonates under reducing redox conditions (Lazar et al., 2014)(in this Special
213 Collection). Dissociation of carbonates in the supercritical aqueous fluid yields dissolved
214 cation (i.e. Ca^{2+}, Mg^{2+}) concentrations comparable to those of $CO_{2(aq)}$.
215
216 **Carbonate Ion in the Melt Structure**
217 Spectroscopic data were collected *in-situ* and *ex-situ* for the fluid, gas, melt and
218 crystalline phases [2]. The C-O-H speciation of the carbonate melts and coexisting
219 supercritical aqueous solutions is mainly H_2O and CO_3^{2-}. These species were identified at
220 the frequency envelopes of 1060 – 1100 cm^{-1} and 3400 – 3600 cm^{-1}, respectively (Fig.
221 3a). The carbonate ion also exhibits the Raman-active in-plane symmetric vibrational
222 band (v_4) at ~ 695 – 725 cm^{-1} (Bates et al., 1972; Carper et al., 2012; Maroni and Cairns,
223 1970). Interestingly, coexisting aqueous fluid appears depleted in dissolved CO_3^{2-} relative
224 to the melt, in accordance with thermodynamic models that suggest predominance
225 presence of $CO_{2(aq)}$ when carbonates equilibrate with aqueous solutions at high
226 temperatures and pressures (Caciagli and Manning, 2003). Even though the Raman

[2] Raw spectroscopic data are available by request (dfoustoukos@ciw.edu)

227 vibrations of the CO_2 fermi-diad (1280 – 1380 cm^{-1}) and C-H stretching band of CH_4
228 (2960 – 2990 cm^{-1}) were not obvious in all the *in-situ* measurements, the *ex-situ* exsolved
229 gas phase was enriched in these C-O-H volatiles (Fig. 3b, c). The carbon speciation of the
230 quenched fluids also included HCO_3^- (ν_1 ~ 1010 cm^{-1} (Frantz, 1998)), reflecting rapid re-
231 equilibration during quenching at pH conditions lower than the pK_1 of HCO_3^-dissociation
232 to CO_3^{2-} (~10.3 at 25°C, 1 bar) (Stumm and Morgan, 1996).

233 Under oxidizing redox conditions imposed by the Re/ReO_2 assemblage, Raman
234 spectra provide evidence for the presence of ionic rhenium species, such as ReO_2^- and
235 ReO_4^- (Fig. 3, 4). Raman spectra reveal that not only the aqueous solution but also both
236 the melt and the quenched carbonate were enriched in rhenium, which marks the
237 enhanced solubility of trace elements and metals in carbonate-bearing melts and
238 carbonatites (Dalou et al., 2009; Dasgupta et al., 2009; Hamilton et al., 1989; Jones et al.,
239 1995; Martin et al., 2013; Veksler et al., 2012; Veksler and Keppler, 2000). The position
240 of the Raman vibration of this rhenium specie resides at ~ 960 cm^{-1}, which is similar to
241 the symmetric stretching bands of ReO_4^-, ReO_2^- and ReO_2 (Gafurov and Aliev, 2005;
242 Zhou et al., 2000). Bands assigned to antisymmetric ν_3 reside at a slightly lower
243 frequency.

244 To constrain better the speciation of rhenium and to characterize the Raman
245 spectra of the Re-bearing system at high pressures and temperatures, a hydrothermal
246 diamond anvil experiment was performed involving the ReO_2-Re-H_2O equilibrium at 500
247 – 900 °C and 945 – 2185 MPa (Table 1). Raman spectra collected closely resemble the
248 symmetric (ν_1 ~ 960 cm^{-1}) and antisymmetric (ν_3 ~ 900 cm^{-1}) stretching vibrations of
249 ReO_4^-/ReO_2^- (Gafurov and Aliev, 2005; Zhou et al., 2000). Characterization of the

250 ReO_4^-/ReO_2^- vibrational spectrum is also important in order to resolve spectral
251 interferences by HCO_3^-. The later, for example, has been shown to register a broad
252 Gaussian C-OH stretching band at lower frequencies (e.g. 948 cm^{-1}, FWHH 72.5 cm^{-1} at
253 548 ^oC) with a strong temperature dependence (Frantz, 1998). The *in-situ* acquired
254 Raman spectra are different from those of the initial and quenched ReO_2 solid reactant
255 (Fig. 4a). The intense Lorentzian band assigned to v_1 decreased slightly from 964 cm^{-1} to
256 960 cm^{-1} with temperature increase, while the FWHH ranged from 10 cm^{-1} at 500 ^oC to
257 15 cm^{-1} at 900 ^oC (Fig. 4b and c). The main 960 cm^{-1} sharp Raman vibron appeared after
258 few hours of reaction at high temperatures and pressures (Table 1). It is attributed to
259 ReO_2^- because of the trace concentrations of ReO_4^- expected at the oxidizing
260 hydrothermal conditions imposed by the Re-ReO_2 redox buffer (Xiong and Wood, 2001).
261 Raman spectra collected in the Ti/TiO_2 – bearing experiments lacked this sharp 960 cm^{-1}
262 vibration (Fig. 3c), indicating that the Re gasket was not altered under reducing redox
263 conditions and supports the assignment of this peak to oxidized rhenium species.
264
265 **The Structure of CO_3^{2-} in the Carbonate Melt**
266 *In-situ* Raman spectra reveal structural differences between the carbonate ions in
267 melt and crystalline phases (Fig. 5). The symmetric stretching vibration of CO_3^{2-} in melts
268 is clearly at lower frequency (~ 10 cm^{-1}) than what is observed for calcite coexisting with
269 melt and the aqueous phase (Fig. 5a, 6b). This frequency difference is similar to data
270 presented in diamond-anvil experimental studies of anhydrous melting of carbonates at
271 high pressures and temperatures (Williams and Knittle, 2003), and it is indicative of the
272 CO_3^{2-} units in a melt (liquid) structure. In contrast to the structure of anhydrous carbonate

273 melts (Williams and Knittle, 2003), however, experimental data did not reveal the
274 presence of C-O single bonded species that have been suggested to express stretching
275 vibrations at a much lower frequency (~ 970 cm^{-1}) (Fig. 5) (Williams and Knittle, 2003).
276 Integration of the band assigned to v_1-CO_3^{2-} required the employment of "high"
277 and "low" frequency Gaussian components (Fig. 5b). Similar structures have been
278 observed in spectra of Na-K-Mg carbonates quenched from high temperature/-pressure
279 (Genge et al., 1995; Shatskiy et al., 2013). These features have been attributed to the
280 coexistence of polymorph phases (Genge et al., 1995). In our experiments, the full width
281 at half height (FWHH) of the high frequency component is within the range of values
282 expected for CO_3^{2-} ions dissolved in supercritical aqueous solutions (Frantz, 1998),
283 whereas the low frequency contribution (melt structure) is broader by 30 – 40 cm^{-1} (Fig.
284 6a). The position of the frequency envelope is also shifted by 30 – 60 cm^{-1} relative to the
285 symmetric stretch of CO_3^{2-} aqueous species (Frantz, 1998) (Fig. 6b). This frequency shift
286 may suggest a stronger C-O bonding environment in the melt, and similar to that of
287 molten and crystalline Na-Li-K-Ca carbonates at high temperatures and pressures (Bates
288 et al., 1972; Kraft et al., 1991; Maroni and Cairns, 1970). Those studies, however, did not
289 report the asymmetry topology of the v_1-CO_3^{2-} observed in our experiments.
290 For the water-saturated carbonate melts of our study (Fig. 3a, 5b), we hypothesize
291 that this low frequency component of the v_1-CO_3^{2-} is because of H_2O that is bonded to the
292 oxygen of the carbonate ion through intermolecular attraction (i.e O=C-O•••H-O).
293 Another possibility is contributions from a O=C-O-H-O bonding environment involving
294 an oxygen that is shared between the carbonate ion and the structural water (O-H groups)
295 in the melt. Analogous oxygen sharing between SiO_4 and CO_3^{2-} groups have been

296 proposed to exist in polymerized carbonate-bearing silicate melts (Brooker et al., 2001;
297 Brooker et al., 1999; Kubicki and Stolper, 1995; Morizet et al., 2010; Mysen et al., 2011).
298 However, a Raman band assigned to stretching vibrations of such a bond would be
299 expressed at significantly lower frequency and probably comparable to the position of the
300 C-O-H in HCO_3^- groups (e.g. 948 cm^{-1}, FWHH 72.5 cm^{-1} at 548 ^oC) (Frantz, 1998). The
301 reason for the asymmetry of the v_1-CO_3^{2-} vibron observed in the recrystallized calcite and
302 magnesite at conditions (Fig. 5b, 6) is not clear and could be of hydrogen bonding effects
303 or due to Raman inferences from the coexisting carbonate melt.
304
305 **The Structure of Water in the Carbonate Melt**
306 Spectroscopic data collected *in-situ* at high temperature/-pressure also provide
307 insights about the structure of water in the Ca/-Mg carbonate melts. The de-convolution
308 of the vibrational frequency envelope between 3400 and 3600 cm^{-1} allows us to assess the
309 relative contribution of the different O-H bonding environments in both the fluid and
310 melt phase. Raman spectra in the aqueous phase are composed of a band ~ 3550 cm^{-1}
311 assigned to O-H stretching in isolated OH-groups (O-H v_1) and of a lower frequency
312 contribution (O-H_{HB} v_1 ~ 3450 cm^{-1}) attributed to O•••H-O bonding induced by the
313 intermolecular coupling and dipole properties of water molecules (Frantz et al., 1993;
314 Walrafen et al., 1986) (Fig. 7). The thermodynamic properties of hydrogen bonding has
315 been studied in supercritical aqueous solutions (Foustoukos and Mysen, 2012) and in
316 hydrated silicate melts (Mysen, 2012; Mysen, 2011), with a strong negative effect of
317 temperature on the stability of the bond.

318 There is a similar asymmetric shape for the O-H intensity envelope in the
319 carbonate melt in the present study. This asymmetry might reflect intermolecular
320 interactions between the dissolved water dipoles (i.e. H-O•••H-O) or the CO_3^{2-} and
321 structural O-H groups (i.e. O=C-O•••H-O) (Fig. 7). Here, however, the asymmetry of the
322 O-H Raman spectra also indicates the existence of one more component at the high end
323 of the frequency envelope (~ 3600 cm^{-1}) (O-H_M, str), which is attributed to the interaction
324 of O-H groups with the cations (M) in the carbonate melt. This band exists regardless of
325 the MgO/-CaO in the reacting mineral assemblage. This vibrational contribution is not
326 evident in the O-H frequency envelope for the coexisting supercritical aqueous fluid. This
327 may be because of the dilute concentrations of dissolved cations (0.01 molal, see
328 discussions earlier). Interestingly, development of hydroxyl bonds between cations and
329 water molecules in the melt has been suggested to affect the alkalinity of the H_2O-
330 enriched melts, enhancing the solubility of REE (Veksler et al., 2012).
331 Analogous bonding environments have also been inferred from Raman spectra of
332 quenched Ca-Al-Na bearing silicate melts (Mysen and Virgo, 1986) and crystalline OH-
333 enriched phases (Aines and Rossman, 1984). In our study, the structure of this M•••O-H
334 contribution probable is a symmetric O-H stretching vibration (A_{1g}), resembling what
335 has been observed and calculated for Mg and Ca-bearing hydroxides (Dawson et al.,
336 1973; Frost, 2011; Reynard and Caracas, 2009; Wang and Andrews, 2005). The presence
337 of portlandite ($Ca(OH)_2$) and brucite ($Mg(OH)_2$) has also been shown to induce a
338 melting-point depression on calcite and magnesite, respectively (Boettcher et al., 1980;
339 Irving and Wyllie, 1975; Walter et al., 1962; Wyllie and Boettcher, 1969; Wyllie and
340 Tuttle, 1959; Wyllie and Tuttle, 1960). However, we did not observe Mg/Ca-hydroxide

recrystallization or exsolution from the melt. Accordingly, this high frequency Raman band is not attributed to crystalline hydroxides coinciding with the melt.

The dominant O-H stretching vibration in the aqueous phase (O-H, ν_1) was integrated with either Lorentzian or Voigt line shape consistent with previous spectroscopic studies in supercritical water (Foustoukos and Mysen, 2012; Maiella et al., 1999), whereas Gaussian functions were chosen for the vibrations of the O-H groups bonded to water dipoles (O-H_{HB} ν_1). The component corresponding to the interaction of the O-H groups with cations dissolved in the melt (O-$H_{,M}$ str) was integrated predominantly with a Gaussian function (Fig. 7). However, for the measurements performed at temperatures greater than 850^{o}C Lorentzian peak functions provided the best statistical fit.

The frequencies and width of the deconvoluted bands from this frequency envelope are strikingly similar to those of water in the aqueous fluid and melt phase (Fig. 8a-d) with the position of the O-H ν_1 band placed between 3520 to 3620 cm^{-1} (Fig. 8a) and the O-H_{HB} ν_1 residing at a slightly lower frequency (Fig. 8b). The O-H stretching band in the melt is 20 - 40 cm^{-1} wider than in the fluid with FWHH values ranging from 160 to 80 cm^{-1} at 600 to 900 ^{o}C, respectively (Fig. 8b). However, the shape of the O-H_{HB} vibron is similar in the two phases (FWHH ~ 350 – 100 cm^{-1}) (Fig. 8d), further suggesting that this bonding environment might correspond mainly to an H-O•••H-O rather than an O=C-O•••H-O intermolecular interaction. To this end, the relative contribution of molecular vs. structural water on the formation of hydrogen bonding cannot be assessed. For all practical purposes, we refer to this bond as O•••H-O in the discussions that follow.

364 The frequency of the O-H_M stretch recorded in the melt is in the narrow range of
365 3600 – 3640 cm^{-1} (Fig. 8e). With temperature increase, the band becomes narrower with
366 FWHH ranging from 80 to 30 cm^{-1} at 600 to 900 ^oC (Fig. 8f). In all cases, the effect of
367 temperature on peak position and shape is similar to that documented in other studies
368 (Foustoukos and Mysen, 2012; Frantz et al., 1993; Mysen, 2012; Mysen, 2011; Walrafen
369 et al., 1986). However, in contrast to water-saturated aluminosilicate melts (Mysen, 2013)
370 the stability of hydrogen bonding (O•••H-O) in the carbonate melt seems to extend to
371 temperatures significantly beyond 400 ^oC.
372
373 **The Thermodynamic Properties and Solubility of Water in the Carbonate Melt**
374 To access the thermodynamic properties of water dissolved in the carbonate melt,
375 the energy required to rapture the O•••H-O bond ($\Delta H_{O\cdots H\text{-}O}$) is estimated adopting the
376 van't Hoff approach employed previously for the stability of hydrogen bonding in
377 supercritical water (Foustoukos and Mysen, 2012; Walrafen, 1968). These calculations
378 derive $\Delta H_{O\cdots H\text{-}O}$ by describing the equilibrium quotient of O•••H-O conversion to isolated
379 O-H bonds in structural water as a linear relationship between the logarithmic values of
380 the relative Raman integrated peak areas and the reverse of absolute temperatures (Fig.
381 9). There is a general trend of decreasing intermolecular interactions as temperature
382 increases, similar to what has been observed for H_2O in silicate melts (Mysen, 2013).
383 However, the O•••H-O in the carbonate melts has an enthalpy of 6.8 ± 1.5 kcal/mol,
384 which is nearly 300 % of the $\Delta H_{O\cdots H\text{-}O}$ calculated for the water present in SiO_2-bearing
385 melts (~ 2.4 ± 0.5 kcal/mol). Accordingly, hydrogen bonding is significantly stronger in
386 carbonate relative to silicate water-saturated melts allowing for the development of more

polar H-bonded water clusters (Schwarzer et al., 2005), and thus, possible enhancing the solubility of ionic species of trace elements and metal in the CO_3^{2-} bearing melt. Interestingly, the energy of the hydrogen bond for the H_2O component of the carbonate melt appears to be comparable with the $\Delta H_{O\bullet\bullet\bullet H\text{-}O}$ in the coexisting supercritical aqueous solution (8.4 ± 1.3 kcal/mol) (Fig. 8), highlighting the significant similarity in the thermodynamic properties of water present in these two phases.

To approximate qualitatively the solubility of H_2O in the carbonate melt, the relative distribution of the integrated peak areas of the O-H and O•••H-O stretching vibrations were used to derive the partition coefficient of H_2O (molecular and structural) present in the coexisting phases ($^{m}_{f}D_{H_2O}$) (Table 2):

$$^{m}_{f}D = \frac{(Area_{O-H}+Area_{O\ldots H-O})_{melt}}{(Area_{O-H}+Area_{O\ldots H-O})_{fluid}} = \frac{X_{melt}}{X_{fluid}} \qquad (1)$$

These estimates assume that the relative normalized differential Raman scattering cross sections (σ_j) of the O-H and O•••H-O v_1 vibrations in the spectra of coexisting melt and aqueous phase at the temperatures and pressures of interest are the same. This assumption is supported by the apparent similarity in the thermodynamic properties of the water solvating in the phases (Fig. 9). The water solubility is enhanced in the Mg-bearing carbonate melt with $^{m}_{f}D_{H_2O}$ values ranging from 0.46 to 0.89 (median = 0.5) at 856 – 900 ^{o}C, 1728 - 2011 MPa (Table 2). In contrast, in the $CaO\text{-}CO_2\text{-}H_2O$ system the smaller partition coefficients (median of 0.3) probable are because of the lower melting temperatures attained.

The only other experimental data available on the solubility of water in Ca-Na-Mg carbonate melts are from Keppler (2003) with a melt water content of nearly 14 wt % at 225 MPa and 900 ^{o}C. In this study, the melt-fluid H_2O partition coefficients attained

values of 0.27 - 0.48, which are comparable to those estimated in our experiments (Table 2). This solubility suggests a greater H_2O melt/fluid partitioning for carbonate melt systems than for water-saturated silicate melts (Behrens, 1995; Burnham and Jahns, 1962; Lesne et al., 2011; Mysen and Acton, 1999; Richet et al., 2000; Tamic et al., 2001).

The solubility data can also provide constrains on the partial molar volume of water ($\overline{V}^{melt}_{H_2O}$) dissolved in melt (Lange, 1995; Mysen, 2007). In detail, this thermodynamic treatment is based on the formulation of $\overline{V}^{melt}_{H_2O}$ as function of the fugacity of pure H_2O ($f^{o}_{H_2O}$) (Haar et al., 1984; Johnson et al., 1992) and the molar fraction of water ($X^{melt}_{H_2O}$) in the melt for the $H_2O_{fluid} = H_2O_{melt}$ equilibrium conditions:

$$\Delta G_T(P) = \Delta G^o_T(1\ bar) + RTln\frac{a^{melt}_{H_2O}}{f^o_{H_2O}} + \int_1^P \overline{V}^{melt}_{H_2O}\, dP = 0 \qquad (2)$$

Here, ΔG_T*(1 bar)* is the Gibbs free energy of solution for H_2O (J/mol) at 1 bar, R is the gas constant, T is temperature (kelvin), and $a^{melt}_{H_2O}$ is the activity of water in the melt. By assuming $a^{melt}_{H_2O} = X^{melt}_{H_2O}$, which implies ideal mixing for the H_2O-carbonate solution (Mysen, 2007), and no pressure effects on the activity coefficient of water dissolved in melt ($\gamma^{melt}_{H_2O}$)(Lange, 1995), we have:

$$ln\frac{f^o_{H_2O}}{X^{melt}_{H_2O}} = \frac{\Delta G^o_T(1\ bar)}{RT} + \frac{\overline{V}^{melt}_{H_2O}}{RT}(P-1) + \ln\gamma^{melt}_{H_2O} \qquad (3)$$

By plotting $\ln f^{o}_{H_2O}/X^{melt}_{H_2O}$ vs. (P-1)/RT, the partial molar of H_2O dissolved in melt is derived as the slope of the linear regression with a value of ~ 48 ± 6 cm^3/mol at 900 ^oC (Fig. 10). Strikingly this estimate is very close to the partial molar volume of supercritical water that ranges from 61.4 to 44 cm^3/mol at 900 ^oC and 150 – 225 MPa (Haar et al., 1984; Johnson et al., 1992). In the case of silicate melts, the partial molar volume of water has been calculated of less than 23 cm^3/mol (1000 ^oC, 1 bar)(Mysen and Acton, 1999; Ochs and Lange, 1999), approximating values of ~ 12 cm^3/mol in aluminum-free melts (Richet et al., 2000) but decreasing to ~ 9 cm^3/mol for aluminum-enriched melt compositions (Mysen, 2007).

Thus, it appears that the H_2O might be a stronger solvent in the structure of CO_3^{2-} melts than when dissolved in silicate melts, contributing to the enhanced solubility of trace elements and metals observed in carbonate-bearing melts (Dalou et al., 2009; Dasgupta et al., 2009; Hamilton et al., 1989; Jones et al., 1995; Martin et al., 2013; Veksler et al., 2012; Veksler and Keppler, 2000). Furthermore, adopting $\overline{V}^{melt}_{H_2O}$ ~ 48 and 13 wt % H_2O_{melt} at 200 MPa, 900 ^oC (Keppler, 2003), the activity coefficient of water dissolved in the carbonate melt is nearly 9, yielding a natural logarithmic value of ~ -6 for the equilibrium constant of $H_2O_{fluid} = H_2O_{melt}$. Thus, the ionic structure of the carbonate-bearing melt might impose a strong "salting-out" effect on the neutral species of H_2O, similar to what has been seeing for neutral non-polar aqueous species (e.g. $H_{2(aq)}$, $H_2S_{(aq)}$) in electrolyte-bearing supercritical solutions (Foustoukos and Seyfried, 2007; Oelkers and Helgeson, 1991; Pitzer and Schreiber, 1987). Nevertheless, the enhanced solubility of H_2O and the development of M•••O-H bonding environment along with the strong ionic nature of the carbonate melts is anticipated to promote the solvation of ionic

453 species (such as ReO_2^-) in the melt structure (Fig. 4) (Veksler et al., 2012; Veksler and
454 Keppler, 2000).
455
456 **IMPLICATIONS**
457 **Hydrous Melting of Carbonates and CO_2 fluxes in Subduction Zones**
458 The existence of a univariant equilibria between carbonates-oxides-hydroxides
459 and fluid/melt at crustal temperatures and pressures (<1 GPa, 900 ^oC) was first
460 hypothesized by Wylie and Tuttle (1960) and Walter et al. (1962). This has been
461 experimentally demonstrated in the present study (Fig. 2b). These melting relationships
462 and pressure-temperature paths for the CaO-CO_2-H_2O and MgO-CO_2-H_2O systems
463 highlight the important role of alkaline earth oxides on the hydrous melting of the
464 carbonate-bearing subducting oceanic crust and the release of $CO_{2(g)}$ in volcanic arcs. To
465 this end, carbonates present in marine sediments (Plank and Langmuir, 1998) or
466 serpentinized peridotites (Kodolanyi et al., 2012) may not survive transfer to sub-arc
467 depths and commence melting before the complete dehydration at the slab-mantle wedge
468 interface. Experimental data suggest that this is may occur even at the subduction zones
469 of Vanuatu, Makran and Central America that register cold to intermediate surface
470 temperatures (Syracuse et al., 2010).
471 Thus, carbonate minerals may not serve as CO_2 storage recycled in the deep
472 mantle (Kerrick and Connolly, 2001), but actually contribute to the volcanic CO_2 flux at
473 the arc through melt/fluid interactions at temperatures and pressures well within the
474 stability field of minerals such as serpentine, amphibole and chlorite. These mineral
475 phases have been shown to facilitate H_2O-saturated melting (Grove et al., 2012; Till et

476 al., 2012). However, the speciation and partitioning of C-O-H volatiles between
477 carbonate melts and supercritical fluids is poorly constrained, and future studies are
478 needed to describe the effect of fluid pH and halogen composition/concentration (e.g.
479 NaCl) on the flux of $CO_{2(g)}$ during open-system water-saturated melting of carbonates.
480

481 **ACKNOWLEDGMENTS**

482 This research was conducted with support from the Carnegie Institution of
483 Washington (DF), the NSF-EAR-1250499 (DF, BM) and the NSF-EAR-0734182 (BM)
484 and a NASA Astrobiology Institute (BM). A grant from the W. M. Keck Foundation
485 supported acquisition of the Jasco IRS-3100 microRaman and the Jasco IMV4000
486 microFTIR spectrometers. Li Zhang synthesized the ^{13}C diamond, and her efforts are
487 greatly appreciated. Discussions with Dr. Michael Bizimis are highly appreciated.

Table 1. Description of the HDAC experiments conducted

Phase	T (^{o}C)	P (MPa)	Redox Control	$\log {}^{*}f_{O_2}$
Calcite – H_2O	700 - 950	784 - 1508	Re/ReO_2	(-13.8) – (-6.8)
Calcite – CaO – H_2O	550 - 650	442 - 2663	Re/ReO_2	(-17.1) – (4.4)
Calcite – CaO – H_2O	600 - 900	892 - 2003	Re/ReO_2	(-9.3) – (2.5)
Calcite – CaO – H_2O	575 - 900	791 - 1283	Ti/TiO_2	(-48.2) – (-32)
Magnesite – H_2O	600 - 900	1045 - 1279	Re/ReO_2	(-6) – (-9.7)
Magnesite – MgO – H_2O	860 - 1050	1789 - 2839	Re/ReO_2	(0) – (4)
Magnesite – MgO – H_2O	400 - 1100	920 - 2439	Ti/TiO_2	(-13.7) – (-2.8)
Re – ReO_2 – H_2O	500 - 900	945 - 2185		(-4.4) – (5.6)

* Calculated based on the thermodynamic data of Knacke et al (1991) and adopting the *density model* theory (Anderson and Crerar, 1993).
Redox reactions: $Re + O_{2\,(g)} = ReO_2$ and $Ti + O_{2(g)} = TiO_2$
f_{O_2} conditions estimated for the Ti/TiO2 redox buffer are the lowest values possible, and not accounting for diffusion of H_2 through the Re gasket at elevated temperatures. In all the Ti-TiO_2 bearing experiments, the presence of reduced volatiles (i.e. H_2, CH_4) was confirmed *in-situ* at T-P by Raman spectroscopy.

488

489

490

Table 2. H_2O partition coefficients between carbonate melts and coexisting supercritical fluids

T (^oC)	P (MPa)	${}^{m}_{f}D_{H_2O}$
	Melt (calcite-CaO)-H_2O	
600	1462	0.45
600	1462	0.20
700	2003	0.52
775	1728	0.36
800	1899	0.28
800	1899	0.37
850	1675	0.27
900	892	0.26
900	892	0.21
700	1117	0.83
	Melt (magnesite – MgO) – H_2O	
856	1728	0.46
856	1728	0.51
860	2011	0.76
880	1726	0.89
910	1677	0.48
	$Ca/Na/MgCO_3$ melt – H_2O (Keppler, 2003)	
900	50	0.27
900	75	0.24
900	100	0.37
900	125	0.35
900	150	0.42
900	175	0.36
900	200	0.45
900	225	0.48

491

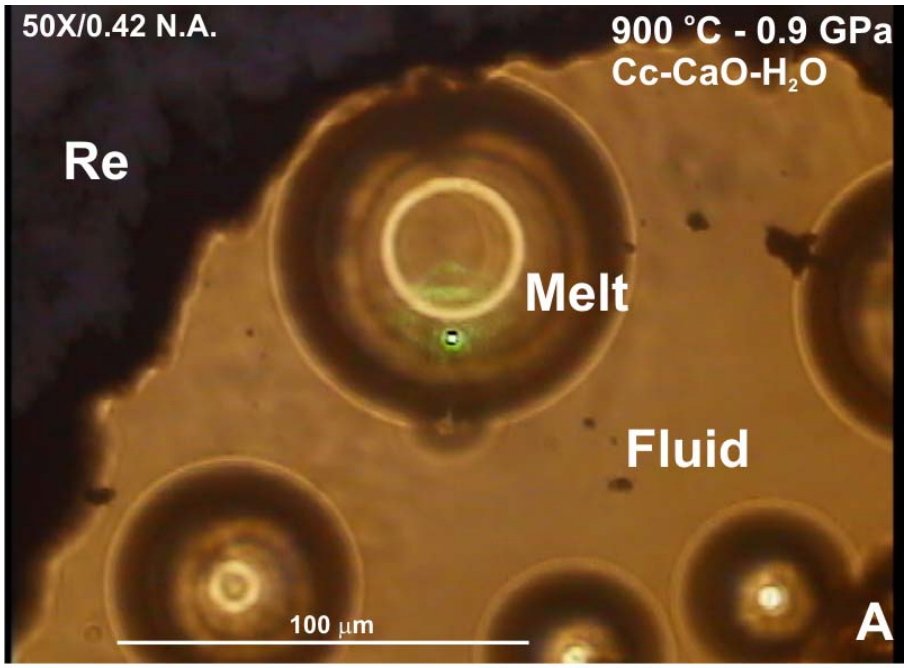

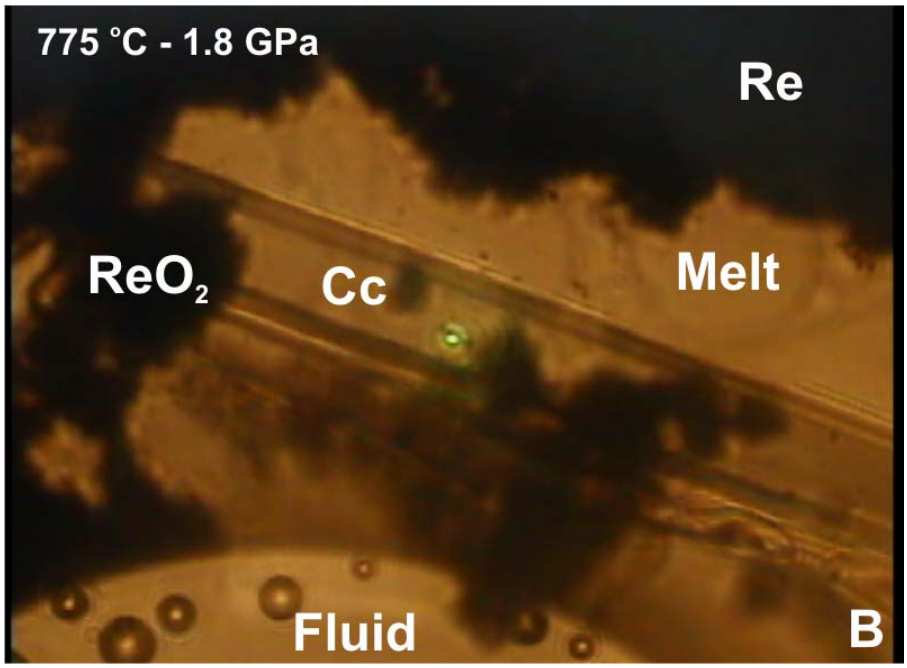

492

493 **Figure 1.** Microphotographs from the high temperature/-pressure HDAC experiments
494 performed to study carbonate (e.g. calcite) melting in the presence of supercritical
495 aqueous solution and under reducing/-oxidizing (e.g. Re/ReO_2) redox conditions.
496 Experiments included fluid, melt, and crystalline phases (oxides, carbonates, Re metal).
497 The size of the excitation laser beam is 1 μm (A).
498
499

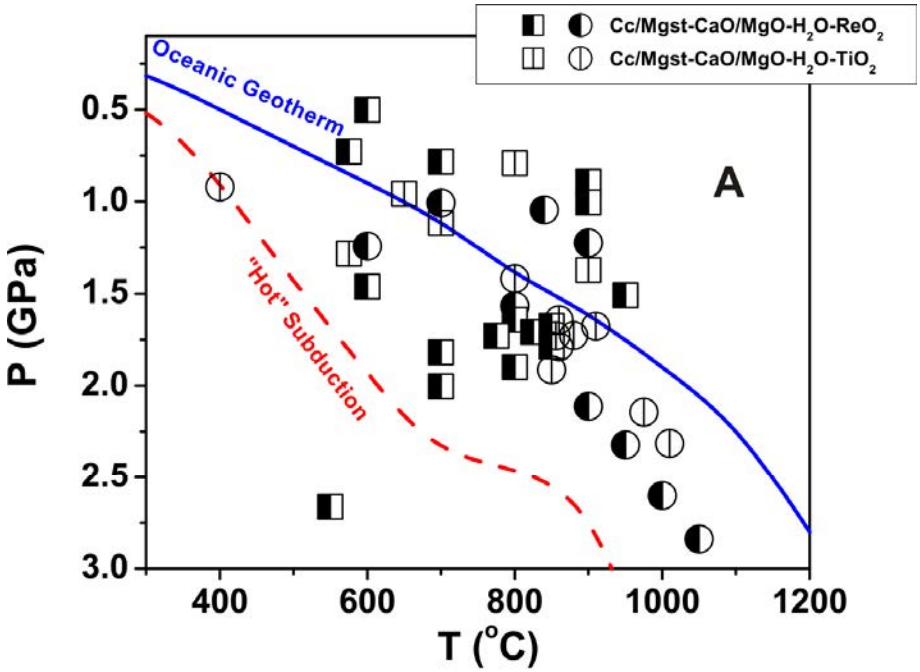

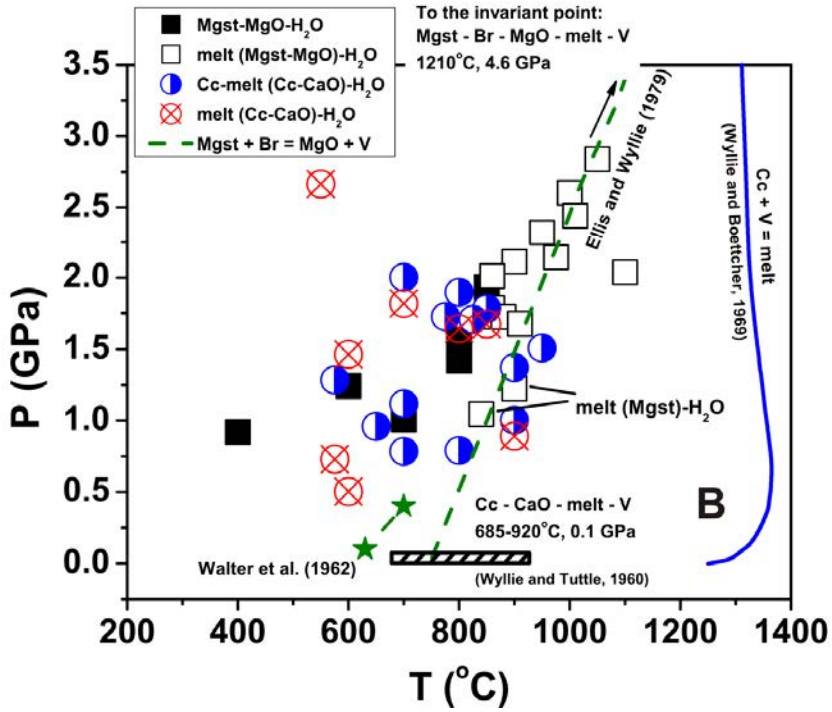

500

Figure 2. (a) Experiments were conducted at temperatures and pressures resembling the oceanic geotherm (a). The "hot subduction" zone is after the D80 model of Central Cascadia (Syracuse et al., 2010) that assumes coupling of the subduction slab with the mantle wedge at 80 km depth. At this transition point and beyond, the subducted sediments are considered fully dehydrated and the extent of hydrous melting is minimal. (b) "In-situ" observations reveal a strong melting-point depression for calcite and magnesite when coexisting with supercritical fluids and CaO or MgO, respectively. The melting relationships identified correspond to conditions similar to those proposed by Wylie and Tuttle (1960), Walter et al. (1962), and Ellis and Wyllie (1979) for the univariant equilibria between carbonates-oxides-hydroxides and fluid/melt.

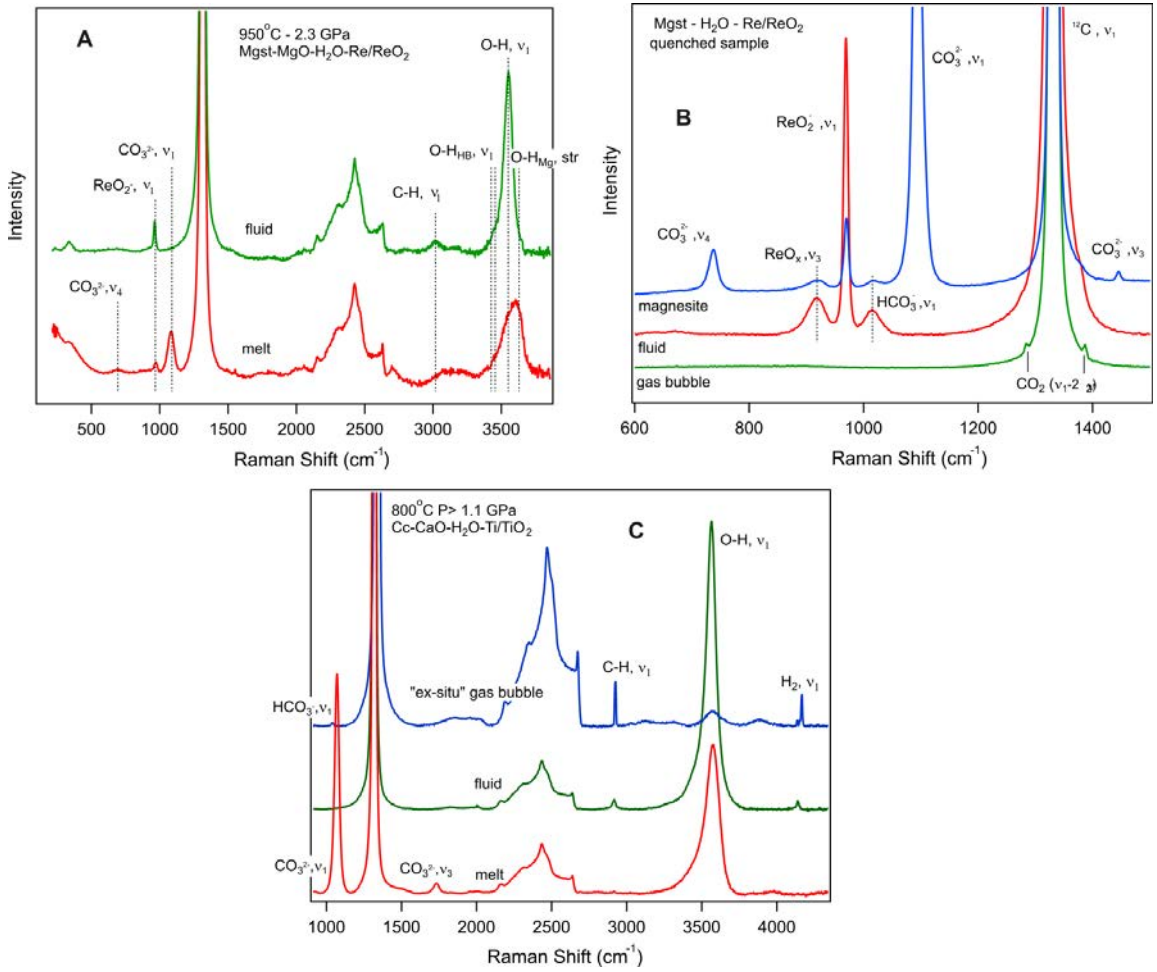

513

Figure 3. Examples of Raman spectra collected *in-situ* at 950 ^{o}C, 2.3 GPa (a), 800^{o}C, >1.1 GPa (c) and for samples quenched from high temperature/-pressure (b). Under oxidizing redox conditions rhenium species (e.g. ReO_2^-) and H_2O are dissolved in both the melt and aqueous phase (a). However, fluids are enriched in $CO_{2(aq)}$ (b), while the melts are composed of CO_3^{2-} ions (a). At reducing conditions established by the Ti/TiO_2 redox buffer, the fluid phase coexisting with the carbonate-bearing melt at high temperatures and pressures is enriched in CH_4 and H_2, but depleted in dissolved rhenium species relative to the melt-fluid equilibrium at oxidizing conditions (a). For "ex-situ" samples, presence of CH_4 and H_2 is evident in the exsolved gas phase (c). The complex group of bands recorded at ~ 2300 - 2800 cm^{-1} corresponds to the second-order Raman scattering (overtones and combination vibrational states) of the ^{12}C diamond anvils (Nemanich and Solin, 1979).

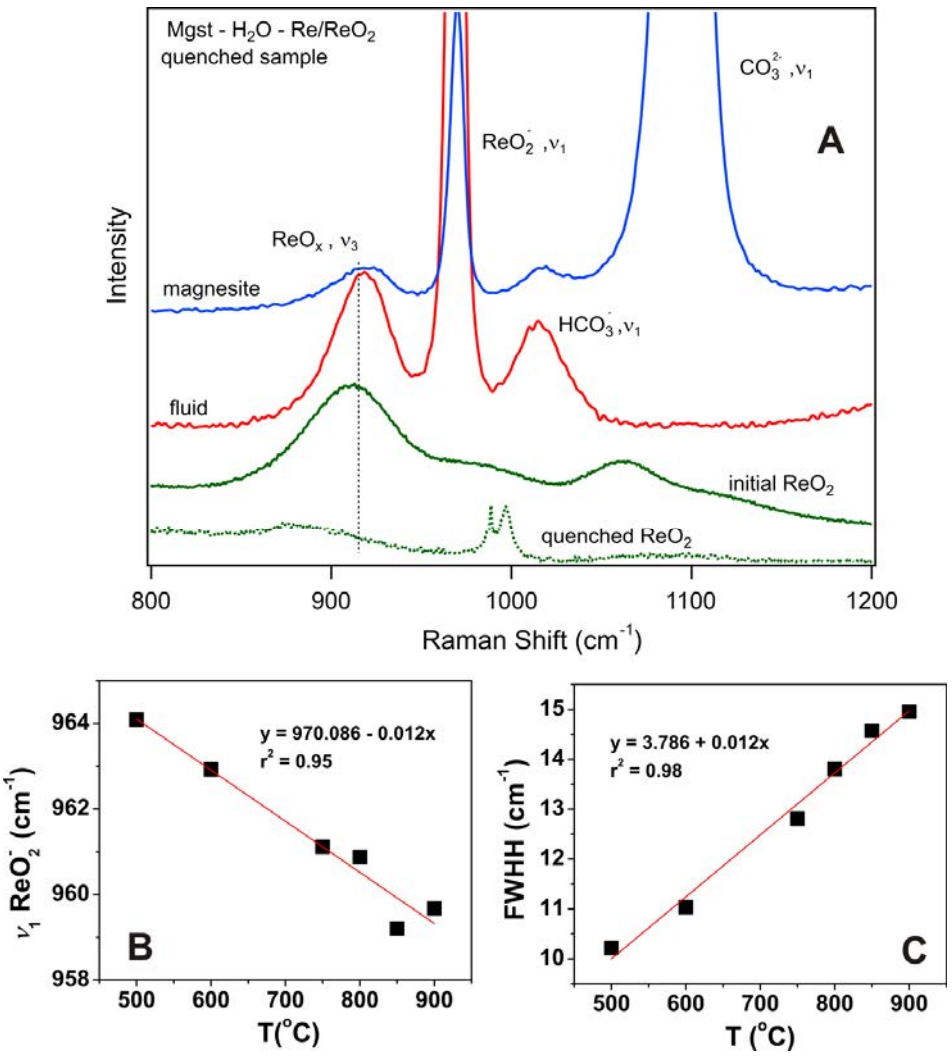

Figure 4. Raman spectra of dissolved rhenium species identified in melt, fluid and precipitated carbonates (a). The intense Lorentzian vibrational band at ~ 960 cm^{-1} does not correlate with the Raman spectrum of the initial and the quenched ReO_2 solid reactant (a). This sharp Raman vibron is attributed to ReO_2^-. A series of HDAC experiments conducted in the Re-ReO_2-H_2O system constrained the effect of temperature on the frequency position (b) and the shape (c) of the ReO_2^- ν_1 stretching band.

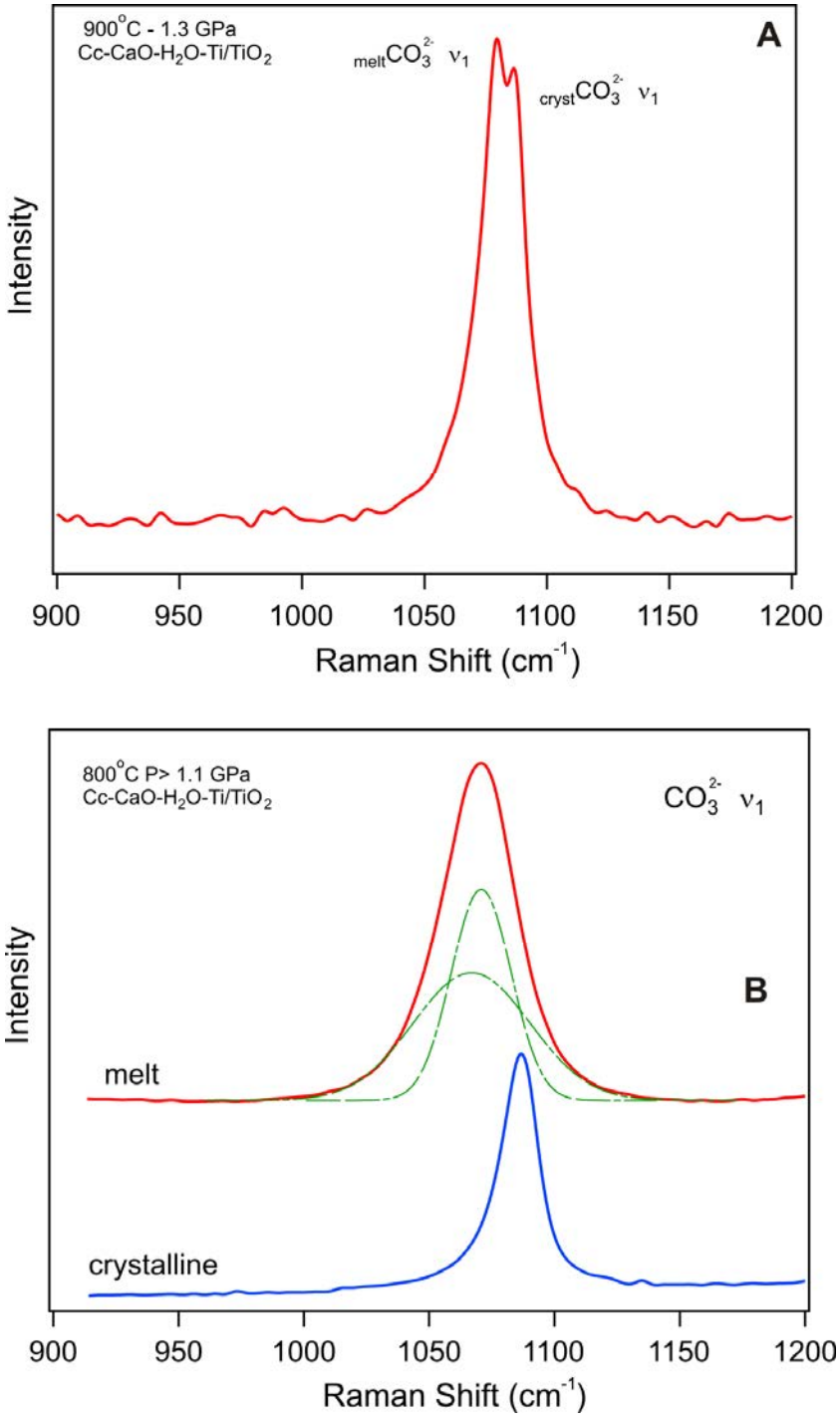

1

Figure 5. Raman spectra collected from $CaCO_3$-CaO-H_2O bearing HDAC experiments at *in-situ* temperatures and pressures a) Spectra of calcite-melt mixtures (red line) reveal that the frequency of the symmetric stretching vibration of CO_3^{2-} is different in spectra of the melt and crystalline phase. b) This is also apparent in Raman measurements of distinct melt (red line) /- crystalline (blue line) carbonate phases. Furthermore, integration of the v_1 band (green line) reveals the presence of a "low" frequency Gaussian component, along with the main frequency contribution, attributed to the hydrogen from the dissolved H_2O bonded to the oxygen of the carbonate ion.

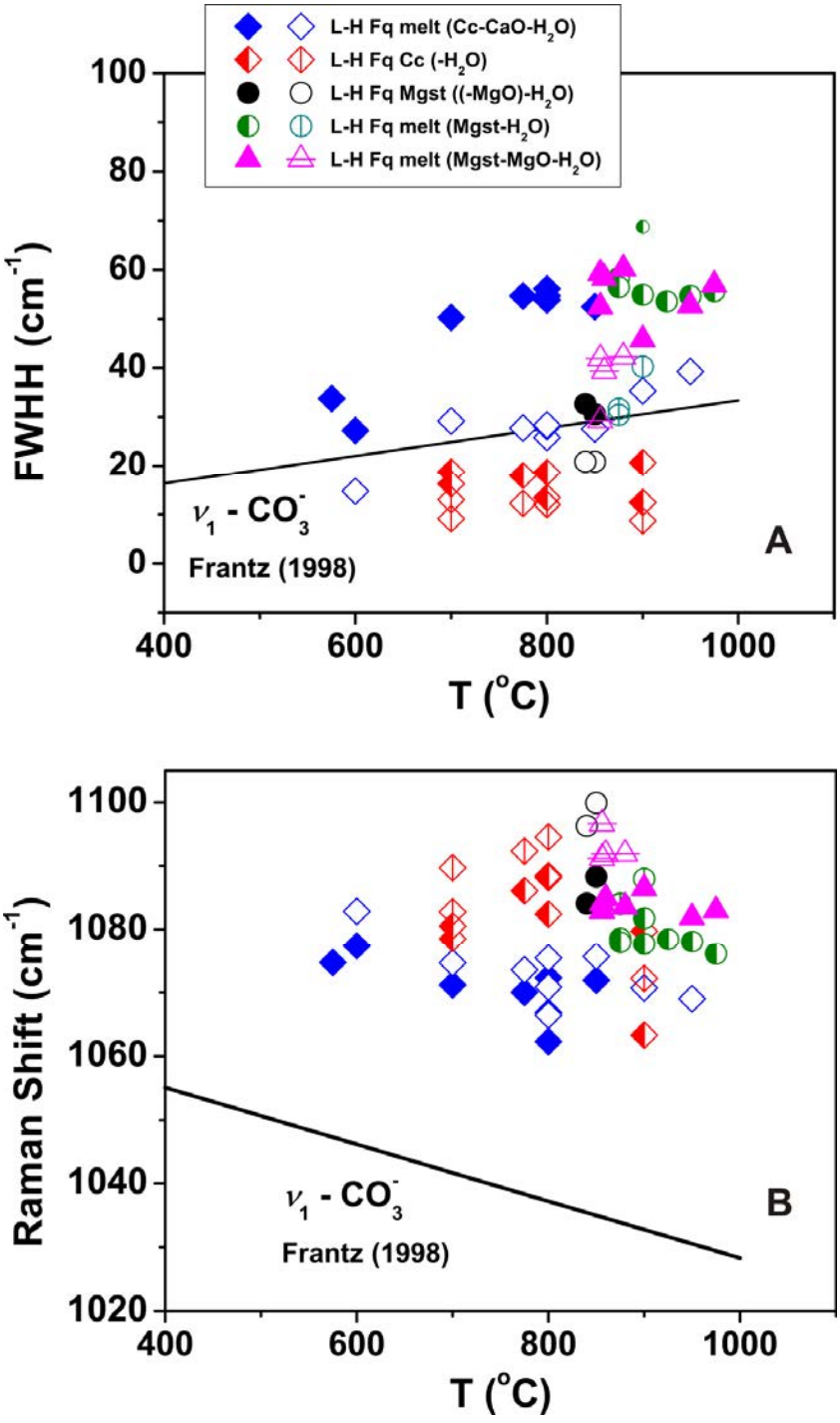

1

Figure 6. The shape (a) and position (b) of the integrated "low" and "high" components of the CO_3^{2-} frequency envelope assigned to the symmetric stretching vibration (ν_1). The molecular and bonding characteristics of the carbonate ion in the melt structure differs greatly from the species dissolved in supercritical aqueous solution (Frantz, 1998).

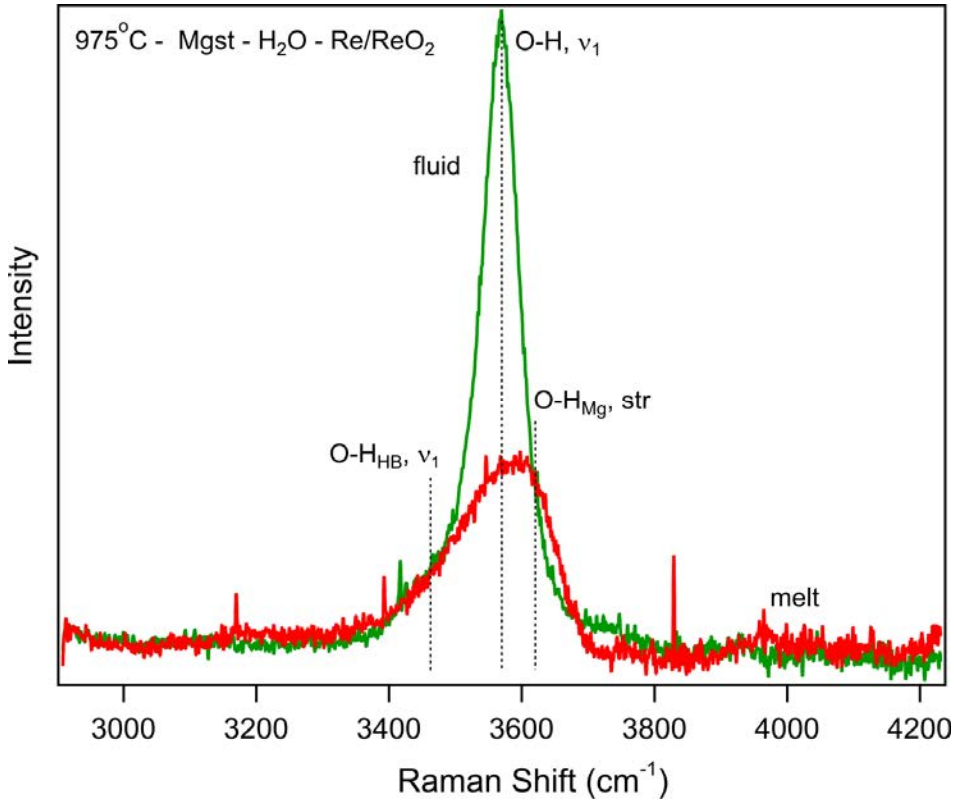

Figure 7. Raman spectra of the 3400 – 3600 cm^{-1} frequency envelope that describes the bulk H_2O composition and the O-H bonding environments in the aqueous and melt phase. Raman spectra include contributions from the isolated O-H bonds (O-H) and from intermolecular interactions between water molecules (hydrogen bonding, $O\text{-}H_{HB}$). In the case of melt, there is one more contribution ($O\text{-}H_{Mg}$) from the interaction of the O-H groups with dissolved in the melt cations (e.g Mg).

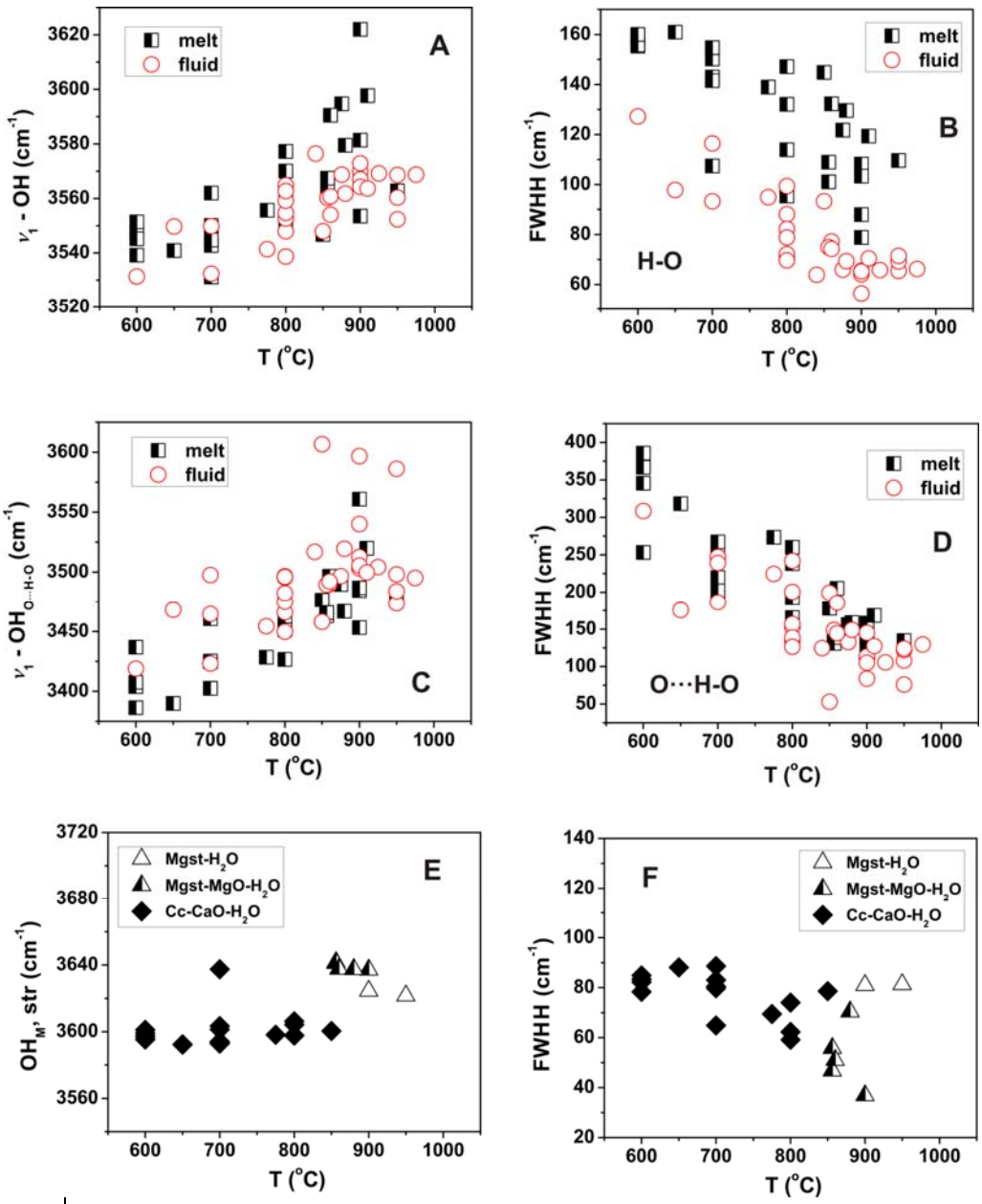

9

Figure 8. The shape (FWHH) and frequency position of the stretching vibrations assigned to the different O-H bonding environments of water dissolved in fluid and melt. The integrated Raman spectra of the O-H frequency envelope at 3400 – 3600 cm^{-1} illustrates the striking similarity of water structure in these two phases (a-d). To this end, the hydrogen bonding contributions in the melt structure are more likely to mainly reflect intermolecular interactions between water dipoles (H-O•••H-O) than between CO_3^{2-} and structural O-H groups (O=C-O•••H-O). With temperature increase, the position of the O-H_M stretch does not shift much and there is a minimal effect on the shape of the band (f).

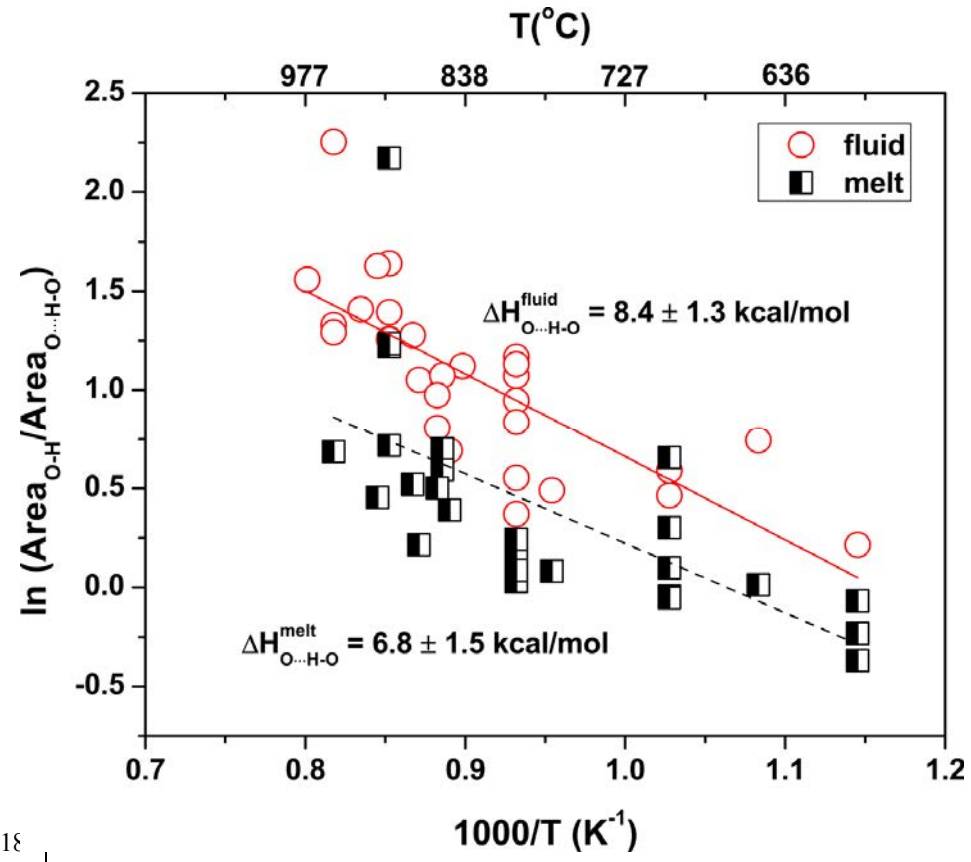

Figure 9. van't Hoff plot for the integrated peak areas of the stretching vibrations of the isolated and hydrogen bonded O-H groups in the carbonate melt and the supercritical aqueous fluid. The slope of the linear regression between $ln(Area_{O\text{-}H}/Area_{O\cdots H\text{-}O})$ vs $1000/T$ corresponds to the enthalpy ($\Delta H_{O\cdots H\text{-}O}$) required to disrupt the intermolecular interaction between water dipoles. Results highlight the similar thermodynamic properties of water dissolved in these two phases. For range of pressure conditions (0.5 – 3 GPa) attained in the present study, the effect of pressure on the stability of intermolecular hydrogen bonding appears to be minimal relative to temperature. Linear regression was performed utilizing the technical graphic and data analysis software *Arc*

1.06 (http://www.stat.umn.edu/arc) (Cook and Weisberg, 1999). The values of 1/(analytical error)^2 were applied as weight (YORK, 1969) and the error in fit parameters of the regression was derived from the covariance matrix as SQRT(cov_{ii}) and for a 95.4% confidence interval. The results of least-squares fitting are considered statistical significant if the two-tail probability (*p-value*) is 0.05 or less (Cook and Weisberg, 1999; Devore, 1995; Press et al., 2007).

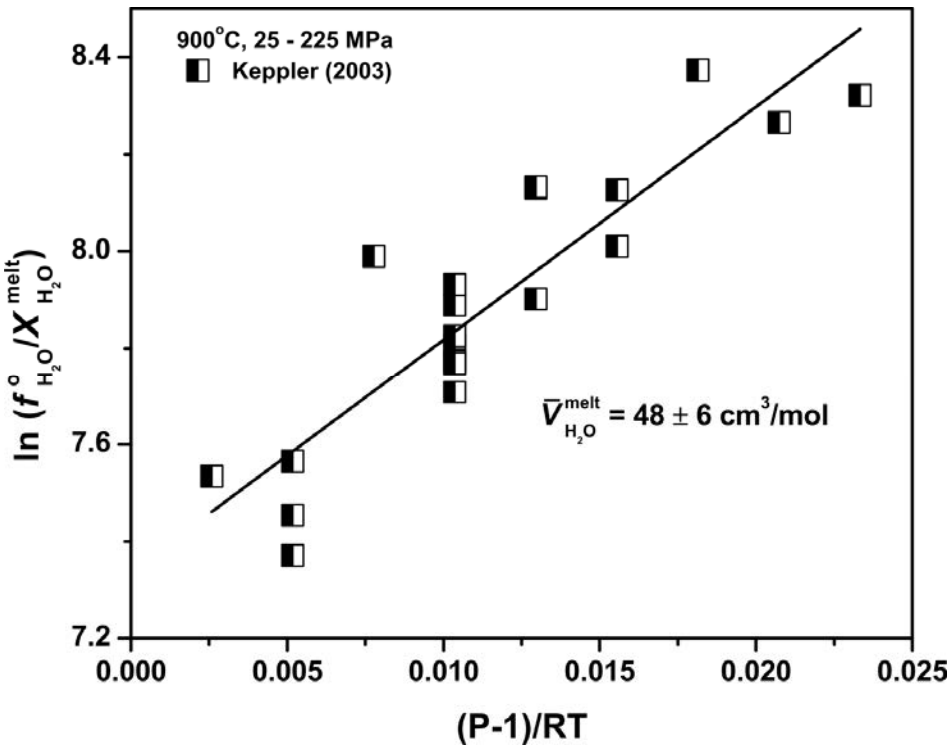

Figure 10. Thermodynamic treatment that estimates the apparent partial molar volume of water ($\bar{V}^{melt}_{H_2O}$) based on water solubility measurements in Na-Ca-Mg carbonate melts that were developed at 900 °C across a pressure gradient (25 to 225 MPa) (Keppler, 2003). The calculated value of ~ 48 ± 6 cm^3/mol is very similar to the partial molar volume of supercritical water at conditions, indicative of strong solvation power for water in the melt structure. The statistical treatment of the linear regression between ln $f^{o}_{H_2O}/X^{melt}_{H_2O}$ vs. (P-1)/RT is described in figure 9.

References:

Aines, R.D., and Rossman, G.R. (1984) Water in minerals - a peak in the infrared. Journal of Geophysical Research, 89, 4059-4071.

Anderson, G.M., and Crerar, D. (1993) Thermodynamics in Geochemistry - The Equilibrium Model. 588 p. Oxford University Press, New York Oxford.

Audétat, A., and Keppler, H. (2005) Solubility of rutile in subduction zone fluids, as determined by experiments in the hydrothermal diamond anvil cell. Earth and Planetary Science Letters, 232(3-4), 393-402.

Bassett, W.A., Wu, T.C., Chou, I.M., Haselton, H.T., Jr., , Frantz, J., Mysen, B.O., Huang, W.L., Sharma, K., and Schiferl, D. (1996) The hydrothermal diamond anvil cell (HDAC) and its applications. In M.D. Dyar, McCammon C., and W.M. Schaefe, Eds. Mineral Spectroscopy: A Tribute to Roger G. Burns. The Geochemical Society Special Publication, No. 5, p. 261-272.

Bates, J.B., Boyd, G.E., Brooker, M.H., and Quist, A.S. (1972) Raman spectra of molten alkali-metal carbonates. Journal of Physical Chemistry, 76(11), 1565-1571.

Behrens, H. (1995) Determination of water solubilities in high-viscosity melts: An experimental-study on $NaAlSi_3O_8$ and $KAlSi_3O_8$ melts. European Journal of Mineralogy, 7(4), 905-920.

Bell, K., and Blenkinsop, J. (1989) Neodymium and strontium isotope geochemistry of carbonatites. In K. Bell, Ed. Carbonatites - Genesis and Evolution, p. 278-300. Unwin Hyman, Boston, Mass.

Bizimis, M., Salters, V.J.M., and Dawson, J.B. (2003) The brevity of carbonatite sources in the mantle: evidence from Hf isotopes. Contributions to Mineralogy and Petrology, 145(3), 281-300.

Boettcher, A.L., Robertson, J.K., and Wyllie, P.J. (1980) Studies in synthetic carbonatite systems - Solidus relationships for CaO-MgO-CO_2-H_2O to 40 Kbar and CaO-MgO-SiO_2-CO_2-H_2O to 10 Kbar. Journal of Geophysical Research, 85, 6937-6943.

Brooker, R.A., Kohn, S.C., Holloway, J.R., and McMillan, P.F. (2001) Structural controls on the solubility of CO2 in silicate melts Part II: IR characteristics of carbonate groups in silicate glasses. Chemical Geology, 174(1-3), 241-254.

Brooker, R.A., Kohn, S.C., Holloway, J.R., McMillan, P.F., and Carroll, M.R. (1999) Solubility, speciation and dissolution mechanisms for CO_2 in melts on the $NaAlO_2$-SiO_2 join. Geochimica et Cosmochimica Acta, 63(21), 3549-3565.

Burnham, C.W., and Jahns, R.H. (1962) A method for determining solubility of water in silicate melts. American Journal of Science, 260(10), 721-745.

Caciagli, N.C., and Manning, C.E. (2003) The solubility of calcite in water at 6-16 kbar and 500-800^{o}C. Contributions to Mineralogy and Petrology, 146(3), 275-285.

Carper, W.R., Wahlbeck, P.G., and Griffiths, T.R. (2012) DFT models of molecular species in carbonate molten salts. Journal of Physical Chemistry B, 116(18), 5559-5567.

Chepurov, A.I., Sonin, V.M., Zhimulev, E.I., Chepurov, A.A., and Tomilenko, A.A. (2011) On the formation of element carbon during decomposition of $CaCO_3$ at high P-T parameters under reducing conditions. Doklady Earth Sciences, 441(2), 1738-1741.

Chou, I.M., Bassett, W.A., and Bai, T.B. (1995) Hydrothermal diamond-anvil cell study of melts - Eutectic melting of the assemblage $Ca(OH)_2$+$CaCO_3$ with excess H_2O and lack of evidence for portlandite-II phase. American Mineralogist, 80(7-8), 865-868.

Cook, D.R., and Weisberg, S. (1999) Applied regression including computing and graphics. 632 p. Wiley-Interscience.

Dalou, C., Koga, K.T., Hammouda, T., and Poitrasson, F. (2009) Trace element partitioning between carbonatitic melts and mantle transition zone minerals: Implications for the source of carbonatites. Geochimica Et Cosmochimica Acta, 73(1), 239-255.

Dasgupta, R., Hirschmann, M.M., McDonough, W.F., Spiegelman, M., and Withers, A.C. (2009) Trace element partitioning between garnet lherzolite and carbonatite at 6.6 and 8.6 GPa with applications to the geochemistry of the mantle and of mantle-derived melts. Chemical Geology, 262(1-2), 57-77.

Dawson, P., Hadfield, C.D., and Wilkinso.Gr. (1973) Polarized Infrared and Raman-Spectra of $Mg(OH)_2$ and $Ca(OH)_2$. Journal of Physics and Chemistry of Solids, 34(7), 1217-1225.

Devore, J.L. (1995) Probability and statistics for engineering and the sciences. Duxbury Press.

Ellis, D.E., and Wyllie, P.J. (1979) Carbonation, hydration, and melting relations in the system MgO-H_2O-CO_2 at pressures up to 100-Kbar. American Mineralogist, 64(1-2), 32-40.

Foustoukos, D.I., and Mysen, B.O. (2012) D/H isotopic fractionation in the H_2-H_2O system at supercritical water conditions: Composition and hydrogen bonding effects Geochimica et Cosmochimica Acta, 86, 88-102.

-. (2013) H/D methane isotopologues dissolved in magmatic fluids: Stable hydrogen isotope fractionations in the Earth's interior. American Mineralogist, 98, 946-954.

Foustoukos, D.I., and Seyfried, W.E. (2007) Fluid phase separation processes in submarine hydrothermal systems. Fluid-Fluid Interactions, 65, 213-239.

Frantz, J.D. (1998) Raman spectra of potassium carbonate and bicarbonate aqueous fluids at elevated temperatures and pressures: comparison with theoretical simulations. Chemical Geology, 152(3-4), 211-225.

Frantz, J.D., Dubessy, J., and Mysen, B.O. (1993) An optical-cell for Raman spectroscopic studies of supercritical fluids and its application to the study of water to 500 ^{o}C and 2000 bar. Chemical Geology, 106(1-2), 9-26.

Frost, R.L. (2011) Raman spectroscopic study of the magnesium carbonate mineral hydromagnesite ($Mg_5[(CO_3)_4(OH)_2].4H_2O$). Journal of Raman Spectroscopy, 42(8), 1690-1694.

Gafurov, M.M., and Aliev, A.R. (2005) Changes in the local symmetry of the ReO_4^- anion near the melting point of alkali metal perrhenates. Journal of Structural Chemistry, 46(5), 824-828.

Genge, M.J., Jones, A.P., and Price, G.D. (1995) An Infrared and Raman-study of carbonate glasses - Implications for the structure of carbonatite magmas. Geochimica Et Cosmochimica Acta, 59(5), 927-937.

Green, D.H., and Ringwood, A.E. (1963a) The genesis of basaltic magmas. Contributions to Mineralogy and Petrology, 15, 103-190.

Green, D.H., and Ringwood, A.E. (1963b) Mineral assemblages in a model mantle composition. Journal of Geophysical Research, 68(3), 937-945.

Grove, T.L., Till, C.B., and Krawczynski, M.J. (2012) The role of H_2O in subduction zone magmatism. Annual Review of Earth and Planetary Sciences, Vol 40, 40, 413-439.

Gudfinnsson, G.H., and Presnall, D.C. (2005) Continuous gradations among primary carbonatitic, kimberlitic, melilititic, basaltic, picritic, and komatiitic melts in equilibrium with garnet lherzolite at 3-8GPa. Journal of Petrology, 46(8), 1645-1659.

Haar, L., Gallagher, J.S., and Kell, G.S. (1984) NBS/NRC steam tables: Thermodynamic and transport properties and computer programs for vapor and liquid states of water in SI units. 320 p.

Hamilton, D.L., Bedson, P., and Esson, J. (1989) The behaviour of trace elements in the evolution of carbonatites. In K. Bell, Ed. Carbonatites: Genesis and Evolution, p. 405-427. Uwin Hyman, London.

Holtz, F., Behrens, H., Dingwell, D.B., and Johannes, W. (1995) H_2O solubility in haplogranitic melts - Compositional, pressure, and temperature dependence. American Mineralogist, 80(1-2), 94-108.

Irving, A.J., and Wyllie, P.J. (1975) Subsolidus and melting relationships for calcite, magnesite and the join $CaCO_3$-$MgCO_3$ to 36 Kb. Geochimica Et Cosmochimica Acta, 39(1), 35-53.

Johnson, J.W., Oelkers, E.H., and Helgeson, H.C. (1992) SUPCRT92 - A software package for calculating the standard molal thermodynamic properties of minerals, gases, aqueous species, and reactions from 1-bar to 5000-bar and 0°C to 1000°C. Computers and Geosciences, 18(7), 899-947.

Jones, A.P., Genge, M., and Carmody, L. (2013) Carbonate melts and carbonatites. Reviews in Mineralogy and Geochemistry, 75, 289-322.

Jones, J.H., Walker, D., Pickett, D.A., Murrell, M.T., and Beattie, P. (1995) Experimental investigations of the partitioning of Nb, Mo, Ba, Ce, Pb, Ra, Th, Pa, and U between immiscible carbonate and silicate liquids. Geochimica Et Cosmochimica Acta, 59(7), 1307-1320.

Keppler, H. (2003) Water solubility in carbonatite melts. American Mineralogist, 88(11-12), 1822-1824.

Kerrick, D.M., and Connolly, J.A.D. (2001) Metamorphic devolatilization of subducted marine sediments and the transport of volatiles into the Earth's mantle. Nature, 411(6835), 293-296.

Knacke, O., Kubaschewski, O., and Hesselmann, K. (1991) Thermochemical properties of inorganic substances. 2412 p. Springer-Verlag, Berlin, Heidelberg.

Kodolanyi, J., Pettke, T., Spandler, C., Kamber, B.S., and Gmeling, K. (2012) Geochemistry of ocean floor and fore-arc serpentinites: Constraints on the ultramafic input to subduction zones. Journal of Petrology, 53(2), 235-270.

Kraft, S., Knittle, E., and Williams, Q. (1991) Carbonate stability in the Earth's mantle - a vibrational spectroscopic study of aragonite and dolomite at high-pressures and temperatures. Journal of Geophysical Research-Solid Earth, 96(B11), 17997-18009.

Kubicki, J.D., and Stolper, D. (1995) Structural roles of CO_2 and CO_3^{2-} in fully polymerized sodium aluminosilicate melts and glasses. Geochimica et Cosmochimica Acta, 59, 683-698.

Lange, R.A. (1995) The effect of H_2O, CO_2 and F on the density and viscocity of silicate melts. In M.R.C.a.J.R. Holloway, Ed. Volatiles in Magmas, 30. Mineralogical Society of America, Washington, DC.

Lazar, C., Zhang, C., Manning, C.E., and Mysen, B.O. (2014) Redox effects on calcite-portlandite-fluid equilibria at forearc conditions: carbon mobility, methanogenesis, and reduction melting of calcite. American Mineralogist, in press.

Lesne, P., Scaillet, B., Pichavant, M., Iacono-Marziano, G., and Beny, J.M. (2011) The H_2O solubility of alkali basaltic melts: an experimental study. Contributions to Mineralogy and Petrology, 162(1), 133-151.

Maiella, P.G., Schoppelrei, J.W., and Brill, T.B. (1999) Spectroscopy of hydrothermal reactions. Part XI: Infrared absorptivity of CO_2 and N_2O in water at elevated temperature and pressure. Applied Spectroscopy, 53(3), 351-355.

Manning, C.E. (2013) Thermodynamic modeling of fluid-rock interaction at mid-crustal to upper-mantle conditions. Reviews in Mineralogy and Geochemistry, 76, 135-164.

Maroni, V.A., and Cairns, E.J. (1970) Raman spectra of fused carbonates. Journal of Chemical Physics, 52(9), 4915-4916.

Martin, L., Schmidt, M., Mattsson, H., and Guenther, D. (2013) Element partitioning between immiscible carbonatite and silicate melts for dry and H_2O-bearing systems at 1-3 GPa. Journal of Petrology, 54(11), 2301-2338.

Morizet, Y., Paris, M., Gaillard, F., and Scaillet, B. (2010) C-O-H fluid solubility in haplobasalt under reducing conditions: An experimental study. Chemical Geology, 279(1-2), 1-16.

Mysen, B. (2012) High-pressure and high-temperature titanium solution mechanisms in silicate-saturated aqueous fluids and hydrous silicate melts. American Mineralogist, 97(7), 1241-1251.

-. (2013) Structure-property relationships of COHN-saturated silicate melt coexisting with COHN fluid: A review of in-situ, high-temperature, high-pressure experiments. Chemical Geology, 346, 113-124.

Mysen, B.O. (2007) The solution behavior of H_2O in peralkaline aluminosilicate melts at high pressure with implications for properties of hydrous melts. Geochimica et Cosmochimica Acta, 71(7), 1820-1834.

-. (2011) An experimental study of phosphorous and aluminosilicate speciation in and partitioning between aqueous fluids and silicate melts determined in-situ at high temperature and pressure. American Mineralogist, 96(10), 1636-1649.

Mysen, B.O., and Acton, M. (1999) Water in H_2O-saturated magma-fluid systems: Solubility behavior in K_2O-Al_2O_3-SiO_2-H_2O to 2.0 GPa and 1300 ^oC. Geochimica Et Cosmochimica Acta, 63(22), 3799-3815.

Mysen, B.O., Kumamoto, K., Cody, G., and Fogel, M. (2011) Solubility and solution mechanisms of C-O-H volatiles in silicate melts with variable redox conditions and melt composition at upper mantle temperatures and pressures. Geochimica et Cosmochimica Acta(75), 6183-6199.

Mysen, B.O., and Virgo, D. (1986) Volatiles in silicate melts at high pressure and temperature: 1. Interaction between OH groups and Si^{4+}, Al^{3+}, Ca^{2+}, Na^{+} and H^{+}. Chemical Geology, 57(3-4), 303-331.

Mysen, B.O., and Yamashita, S. (2010) Speciation and solubility of reduced C-O-H fluids in coexisting fluids and silicate melts determined in situ to 1.45 GPa and 800°C. Geochimica et Cosmochimica Acta, 74, 4577-4588.

Nelson, D.R., Chivas, A.R., Chappell, B.W., and Mcculloch, M.T. (1988) Geochemical and isotopic systematics in carbonatites and implications for the evolution of ocean-island sources. Geochimica Et Cosmochimica Acta, 52(1), 1-17.

Nemanich, R.J., and Solin, S.A. (1979) First-order and second-order raman-scattering from finite-size crystals of graphite. Physical Review B, 20(2), 392-401.

Ochs, F.A., and Lange, R.A. (1999) The density of hydrous magmatic liquids. Science, 283(5406), 1314-1317.

Oelkers, E.H., and Helgeson, H.C. (1991) Calculation of activity coefficients and degrees of formation of neutral ion pairs in supercritical electrolyte solutions. Geochimica et Cosmochimica Acta, 55(5), 1235-51.

Pan, D., Spanu, L., Harrison, B., Sverjensky, D.A., and Galli, G. (2013) Dielectric properties of water under extreme conditions and transport of carbonates in the deep Earth. Proceedings of the National Academy of Sciences of the United States of America, 110(17), 6646-6650.

Pitzer, K.S., and Schreiber, D.R. (1987) The restricted primitive model for ionic fluids: properties of the vapor and the critical region. Molecular Physics, 60, 1067-1078.

Plank, T., and Langmuir, C.H. (1998) The chemical composition of subducting sediment and its consequences for the crust and mantle. Chemical Geology, 145(3-4), 325-394.

Press, W.H., Teukolsky, S.A., Vetterling, W.T., and Flannery, B.P. (2007) Numerical recipes in C: The art of scientific computing. 1256 p. Cambridge University Press, p. 661-666.

Reynard, B., and Caracas, R. (2009) D/H isotopic fractionation between brucite $Mg(OH)_2$ and water from first-principles vibrational modeling. Chemical Geology, 262(3-4), 159-168.

Richet, P., Whittington, A., Holtz, F., Behrens, H., Ohlhorst, S., and Wilke, M. (2000) Water and the density of silicate glasses. Contributions to Mineralogy and Petrology, 138(4), 337-347.

Schiferl, D., Nicol, M., Zaug, J.M., Sharma, S.K., Cooney, T.F., Wang, S.-Y., Anthony, T.R., and Fleischer, J.F. (1997) The diamond $^{13}C/^{12}C$ isotope Raman pressure sensor system for high temperature/pressure diamond-anvil cells with reactive samples. . Journal of Applied Physics, 82, 3256-3265.

Schwarzer, D., Lindner, J., and Vohringer, P. (2005) Energy relaxation versus spectral diffusion of the OH-stretching vibration of HOD in liquid-to-supercritical deuterated water. Journal of Chemical Physics, 123(16), 161105.

Shatskiy, A., Gavryushkin, P.N., Sharygin, I.S., Litasov, K.D., Kupriyanov, I., Higo, Y., Borzdov, Y.M., Funakoshi, K., Palyanov, Y.N., and Ohtani, E. (2013) Melting and subsolidus phase relations in the system Na_2CO_3-$MgCO_3$±H_2O at 6 GPa and the stability of $Na_2Mg(CO_3)_2$ in the upper mantle. American Mineralogist, 98, 2172-2182.

Streckeisen. (1980) Classification and nomeclature of volcanic rocks, lamprophyres, carbonatites and melilitic rocks. IUGS Subcommission on the systematics of Igneous Rocks. Geol Rundsch, 69, 194-207.

Stumm, W., and Morgan, J. (1996) Aquatic Chemistry. Wiley-Interscience, 3rd edition.

Syracuse, E.M., van Keken, P.E., and Abers, G.A. (2010) The global range of subduction zone thermal models. Physics of the Earth and Planetary Interiors, 183(1-2), 73-90.

Tamic, N., Behrens, H., and Holtz, F. (2001) The solubility of H_2O and CO_2 in rhyolitic melts in equilibrium with a mixed CO_2-H_2O fluid phase. Chemical Geology, 174(1-3), 333-347.

Till, C.B., Grove, T.L., and Withers, A.C. (2012) The beginnings of hydrous mantle wedge melting. Contributions to Mineralogy and Petrology, 163(4), 669-688.

Tropper, P., and Manning, C.E. (2005) Very low solubility of rutile in H2O at high pressure and temperature, and its implications for Ti mobility in subduction zones. American Mineralogist, 90(2-3), 502-505.

Veksler, I.V., Dorfman, A.M., Dulski, P., Kamenetsky, V.S., Danyushevsky, L.V., Jeffries, T., and Dingwell, D.B. (2012) Partitioning of elements between silicate melt and immiscible fluoride, chloride, carbonate, phosphate and sulfate melts, with implications to the origin of natrocarbonatite. Geochimica Et Cosmochimica Acta, 79, 20-40.

Veksler, I.V., and Keppler, H. (2000) Partitioning of Mg, Ca, and Na between carbonatite melt and hydrous fluid at 0.1-0.2 GPa. Contributions to Mineralogy and Petrology, 138(1), 27-34.

Walrafen, G.E. (1968) Raman Spectral Studies of HDO in H_2O. Journal of Chemical Physics, 48(1), 244-251.

Walrafen, G.E., Fisher, M.R., Hokmabadi, M.S., and Yang, W.H. (1986) Temperature dependence of the low-frequency and high-frequency Raman scattering from liquid water. Journal of Chemical Physics, 85(12), 6970-6982.

Walter, L.S., Wyllie, P.J., and Tuttle, O.F. (1962) The System MgO-CO_2-H_2O at high pressures and temperatures. Journal of Petrology, 3(1), 49-64.

Wang, X.F., and Andrews, L. (2005) Infrared spectra and electronic structure calculations for the group 2 metal $M(OH)_2$ dihydroxide molecules. Journal of Physical Chemistry A, 109(12), 2782-2792.

Williams, Q., and Knittle, E. (2003) Structural complexity in carbonatite liquid at high pressures. Geophysical Research Letters, 30(1), doi:10.1029/2001gl013876.

Wyllie, P.J., and Boettcher, A.L. (1969) Liquidus phase relationships in system CaO-CO_2-H_2O to 40 kilobars pressure with petrological applications. American Journal Of Science, 267, 489-508.

Wyllie, P.J., and Tuttle, O.F. (1959) Melting of calcite in the presence of water. American Mineralogist, 44(3-4), 453-459.

-. (1960) The system CaO-CO_2-H_2O and the origin of carbonatites. Journal Of Petrology, 1(1), 1-46.

Xiong, Y., and Wood, S.A. (2001) Hydrothermal transport and deposition of rhenium under subcritical conditions (up to 200 ^{o}C) in light of experimental studies. Economic Geology and the Bulletin of the Society of Economic Geologists, 96(6), 1429-1444.

317 Xiong, Y.L., and Wood, S.A. (1999) Experimental determination of the solubility of
318 ReO_2 and the dominant oxidation state of rhenium in hydrothermal solutions.
319 Chemical Geology, 158(3-4), 245-256.
320 Zarzycki, J. (1961) High-temperature X-Ray diffraction studies of fused salts - Structure
321 of molten alkali carbonates and sulphates. Discussions of the Faraday Society(32),
322 38-48.
323 Zhou, M.F., Citra, A., Liang, B.Y., and Andrews, L. (2000) Infrared spectra and density
324 functional calculations of MO_2, MO_3, $(O_2)MO_2$, MO_4, MO_2^- (M = Re, Ru, Os)
325 and ReO_3^-, ReO_4^- in solid neon and argon. Journal of Physical Chemistry A,
326 104(16), 3457-3465.
327
328

50X/0.42 N.A.

900 °C - 0.9 GPa
Cc-CaO-H_2O

Re

Melt

Fluid

100 μm

A

775 °C - 1.8 GPa

Re

ReO_2

Cc

Melt

Fluid

B

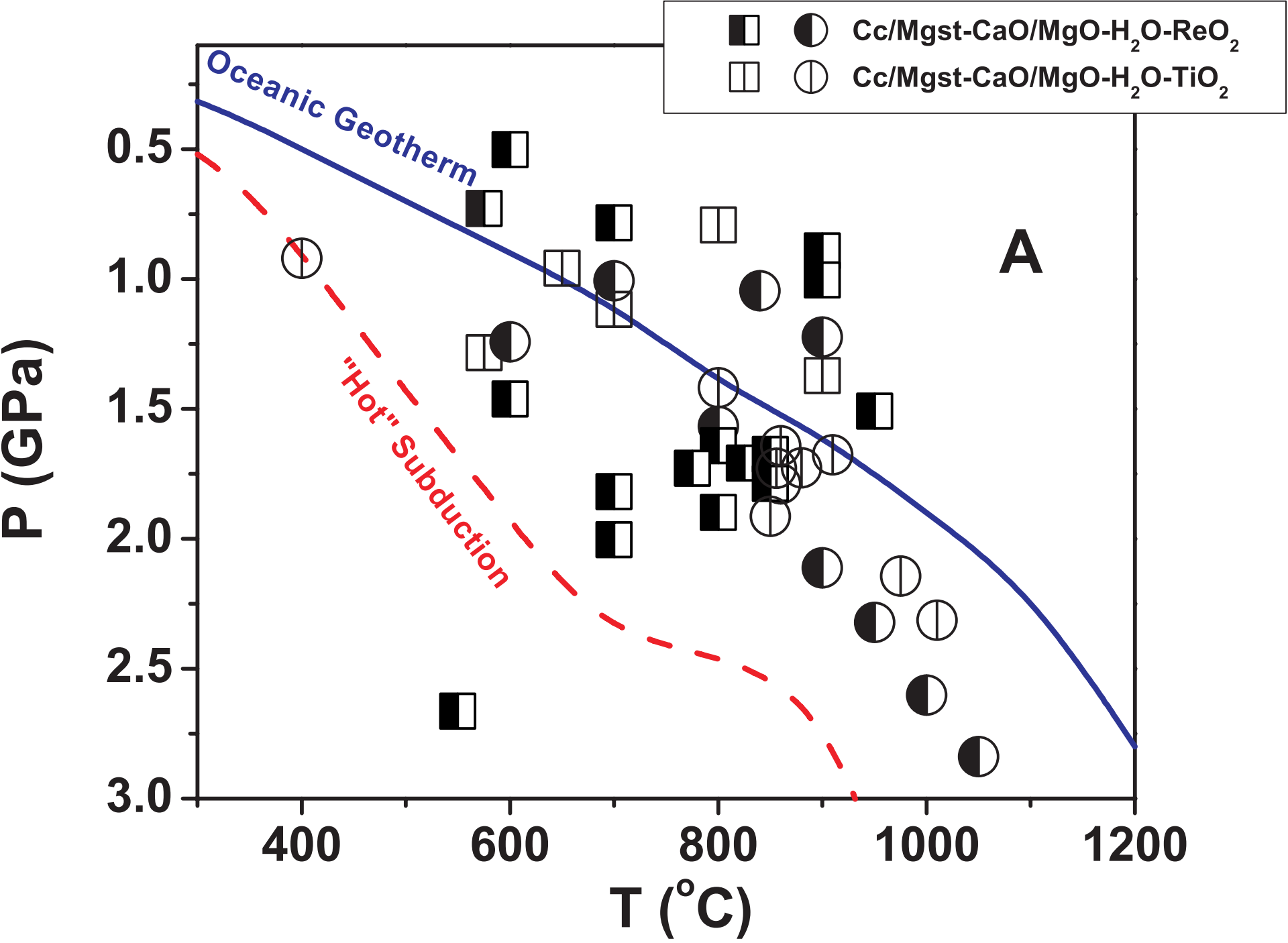
Cc/Mgst-CaO/MgO-H2O-ReO2
Cc/Mgst-CaO/MgO-H2O-TiO2
Oceanic Geotherm
"Hot" Subduction
A
P (GPa)
0.5
1.0
1.5
2.0
2.5
3.0
400
600
800
1000
1200
T (°C)

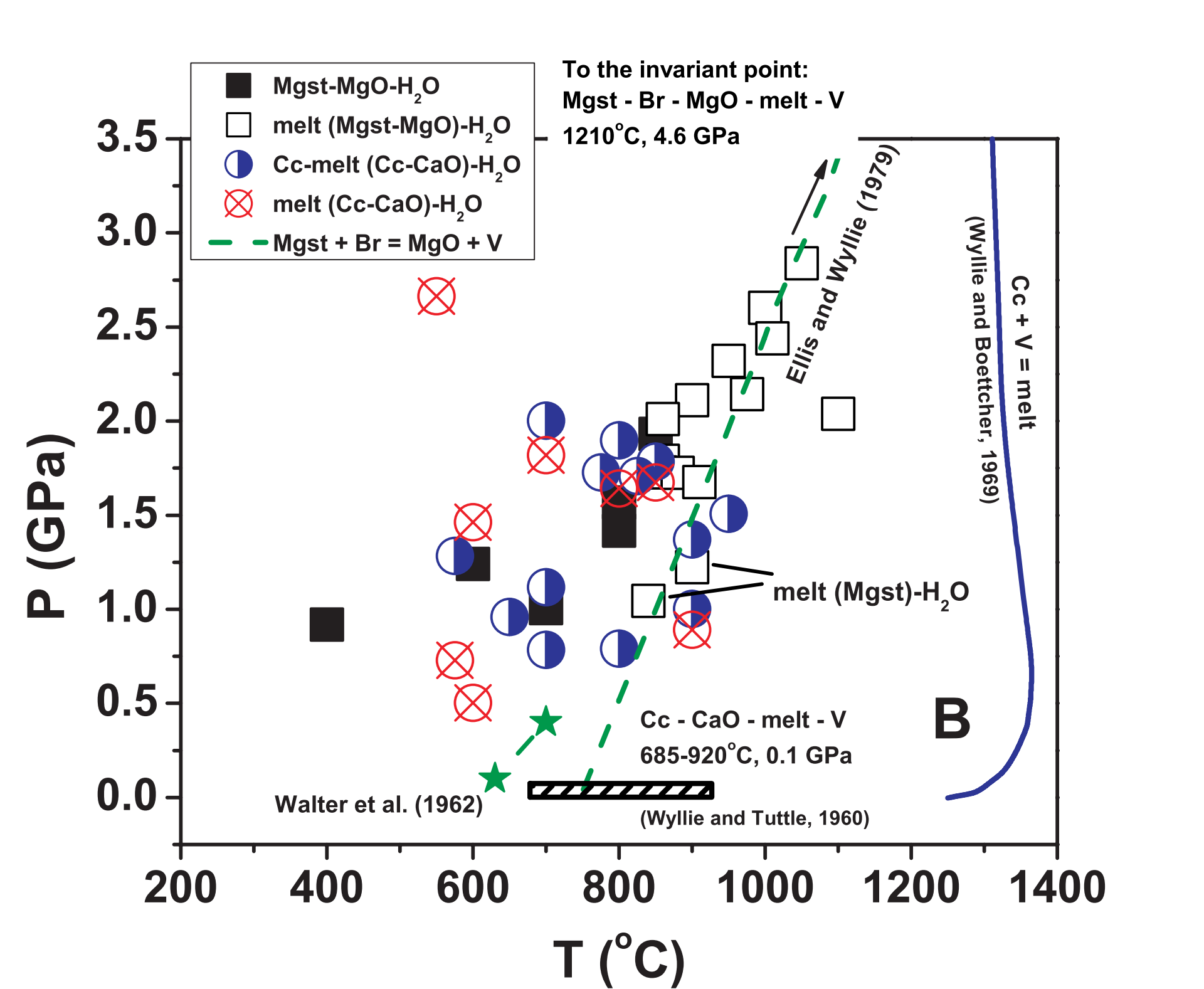
Mgst-MgO-H2O
melt (Mgst-MgO)-H2O
Cc-melt (Cc-CaO)-H2O
melt (Cc-CaO)-H2O
Mgst + Br = MgO + V
To the invariant point:
Mgst - Br - MgO - melt - V
1210°C, 4.6 GPa
Ellis and Wyllie (1979)
(Wyllie and Boettcher, 1969)
Cc + V = melt
melt (Mgst)-H2O
Cc - CaO - melt - V
685-920°C, 0.1 GPa
B
Walter et al. (1962)
(Wyllie and Tuttle, 1960)
P (GPa)
0.0
0.5
1.0
1.5
2.0
2.5
3.0
3.5
200
400
600
800
1000
1200
1400
T (°C)

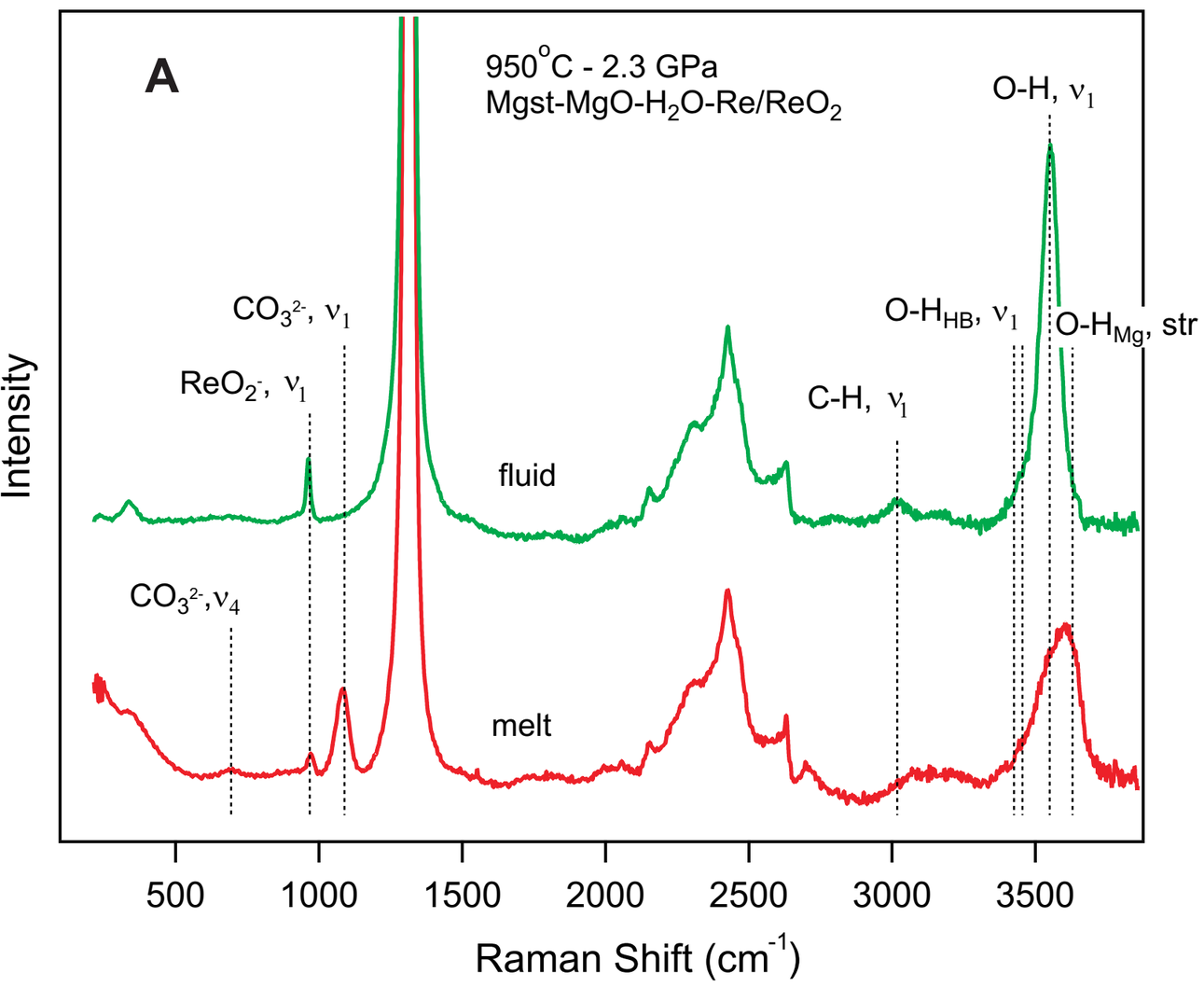
A
950°C - 2.3 GPa
Mgst-MgO-H2O-Re/ReO2
O-H, ν1
CO3 2-, ν1
ReO2-, ν1
O-HHB, ν1
O-HMg, str
C-H, ν1
fluid
CO3 2-,ν4
melt
Intensity
500
1000
1500
2000
2500
3000
3500
Raman Shift (cm-1)

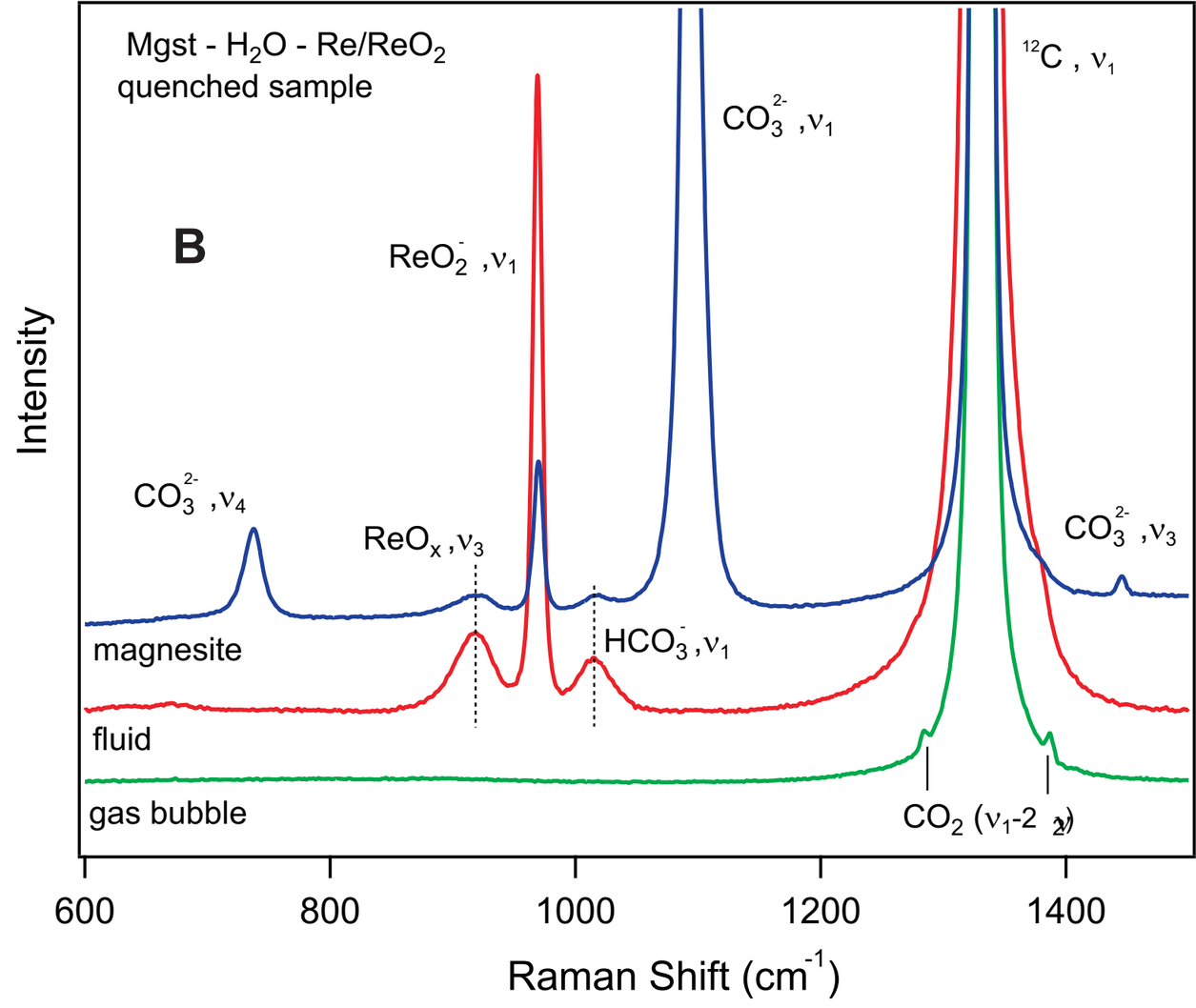
Mgst - H2O - Re/ReO2
quenched sample
B
12C , ν1
CO3 2- ,ν1
ReO2- ,ν1
CO3 2- ,ν4
ReOx ,ν3
CO3 2- ,ν3
HCO3- ,ν1
magnesite
fluid
gas bubble
CO2 (ν1-2 ν2)
Intensity
600
800
1000
1200
1400
Raman Shift (cm-1)

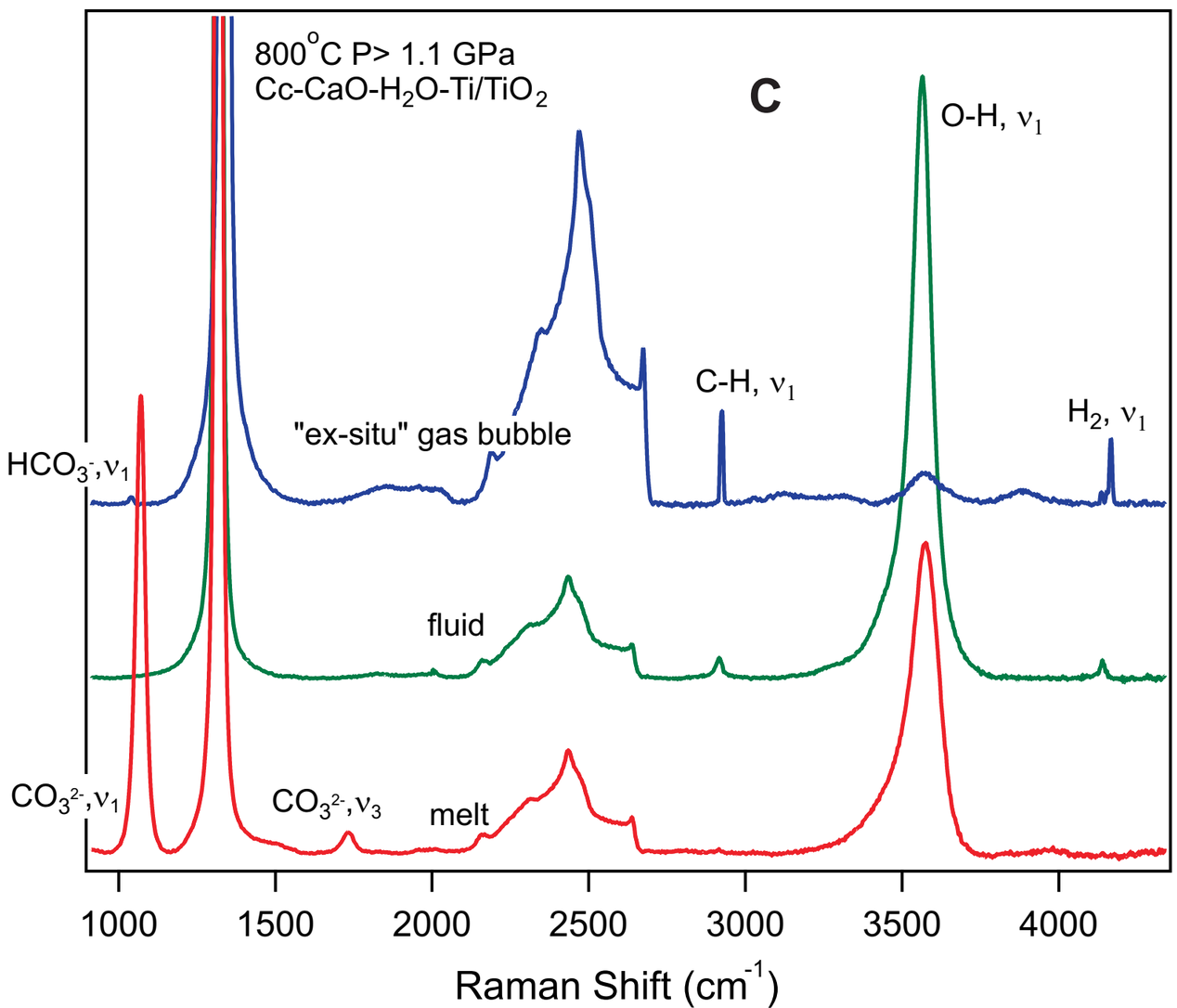
800°C P> 1.1 GPa
Cc-CaO-H2O-Ti/TiO2
C
O-H, ν1
C-H, ν1
H2, ν1
"ex-situ" gas bubble
HCO3-,ν1
fluid
CO3 2-,ν1
CO3 2-,ν3
melt
1000
1500
2000
2500
3000
3500
4000
Raman Shift (cm-1)

Mgst - H_2O - Re/ReO_2
quenched sample

CO_3^{2-} , ν_1

ReO_2^- , ν_1

A

ReO_x , ν_3

magnesite

HCO_3^- , ν_1

fluid

initial ReO_2

quenched ReO_2

Intensity

800 900 1000 1100 1200

Raman Shift (cm^{-1})

ν_1 ReO_2^- (cm^{-1})

y = 970.086 - 0.012x
r^2 = 0.95

B

T($^\circ$C)

FWHH (cm^{-1})

y = 3.786 + 0.012x
r^2 = 0.98

C

T ($^\circ$C)

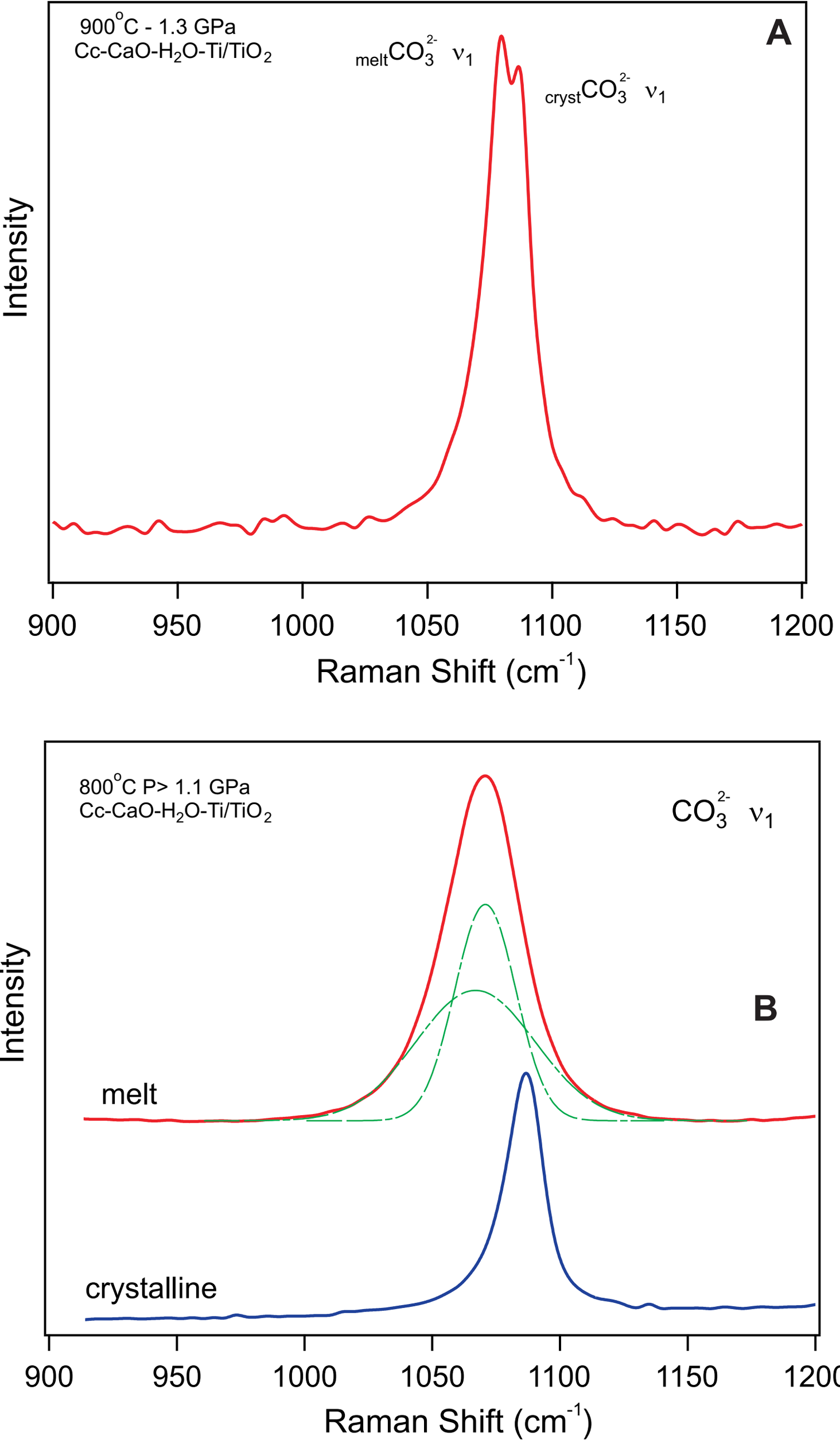
900°C - 1.3 GPa
Cc-CaO-H2O-Ti/TiO2
A
meltCO3 2- ν1
crystCO3 2- ν1
Intensity
900
950
1000
1050
1100
1150
1200
Raman Shift (cm-1)
800°C P> 1.1 GPa
Cc-CaO-H2O-Ti/TiO2
CO3 2- ν1
B
melt
crystalline
Intensity
900
950
1000
1050
1100
1150
1200
Raman Shift (cm-1)

L-H Fq melt (Cc-CaO-H_2O)
L-H Fq Cc (-H_2O)
L-H Fq Mgst ((-MgO)-H_2O)
L-H Fq melt (Mgst-H_2O)
L-H Fq melt (Mgst-MgO-H_2O)

FWHH (cm^{-1})

100
80
60
40
20
0

ν_1 - CO_3^-

Frantz (1998)

A

400
600
800
1000

T (^oC)

Raman Shift (cm^{-1})

1100
1080
1060
1040
1020

ν_1 - CO_3^-

Frantz (1998)

B

400
600
800
1000

T (^oC)

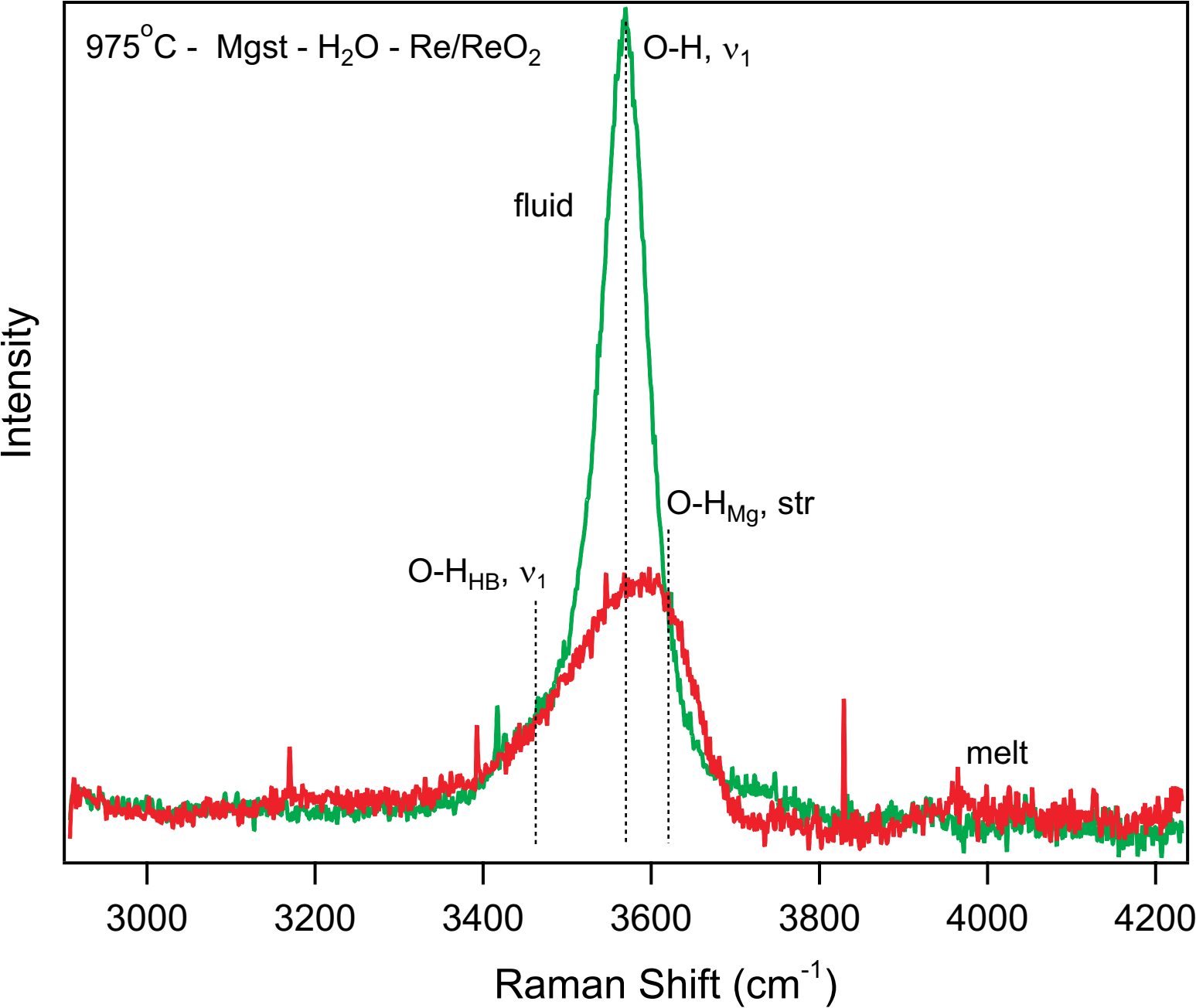
975°C - Mgst - H2O - Re/ReO2
O-H, ν1
fluid
O-HMg, str
O-HHB, ν1
melt
Intensity
3000
3200
3400
3600
3800
4000
4200
Raman Shift (cm-1)

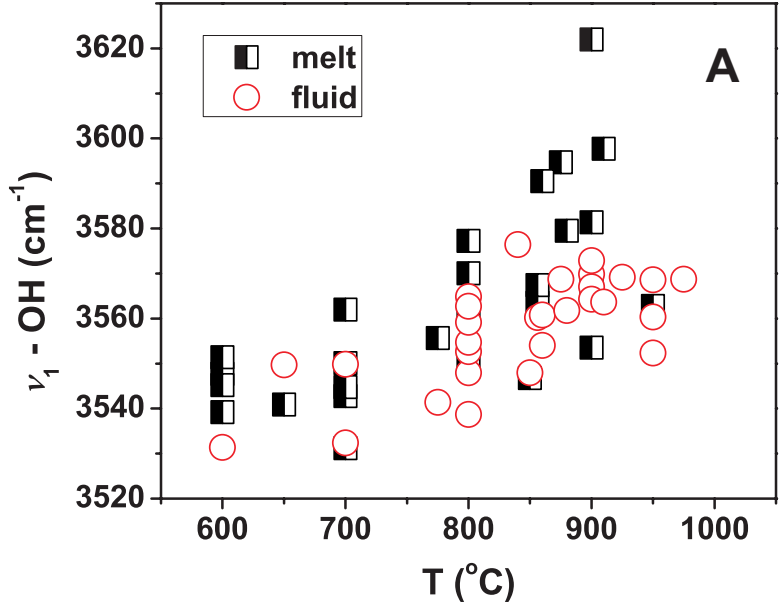
melt
fluid
A
ν_1 - OH (cm^{-1})
T (°C)

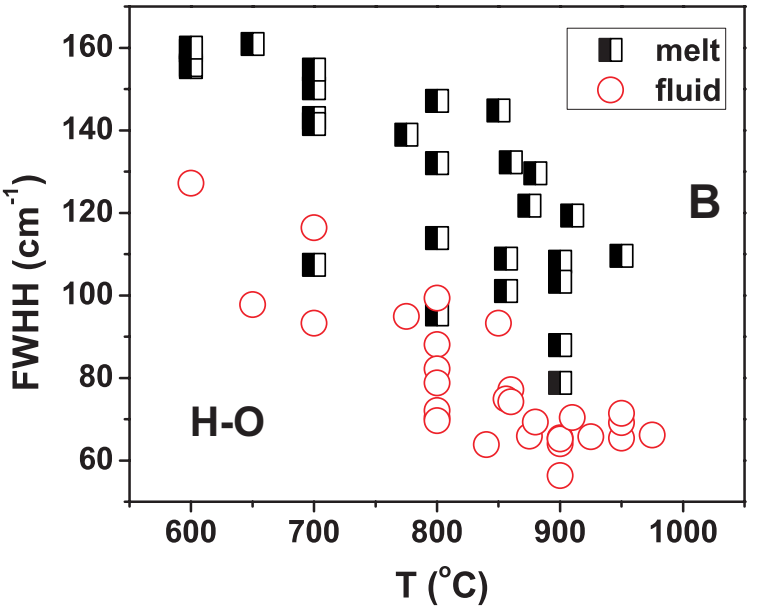
melt
fluid
B
H-O
FWHH (cm^{-1})
T (°C)

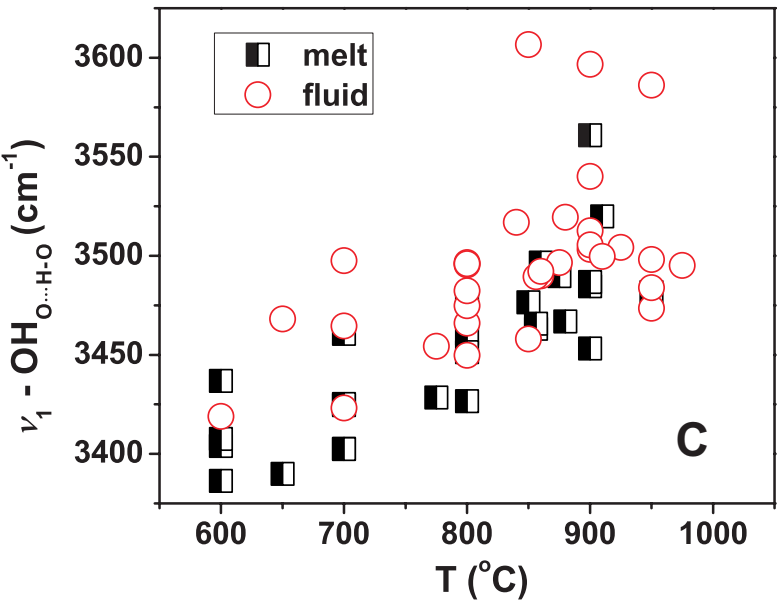
melt
fluid
C
ν_1 - OH$_{O\cdots H\text{-}O}$ (cm^{-1})
T (°C)

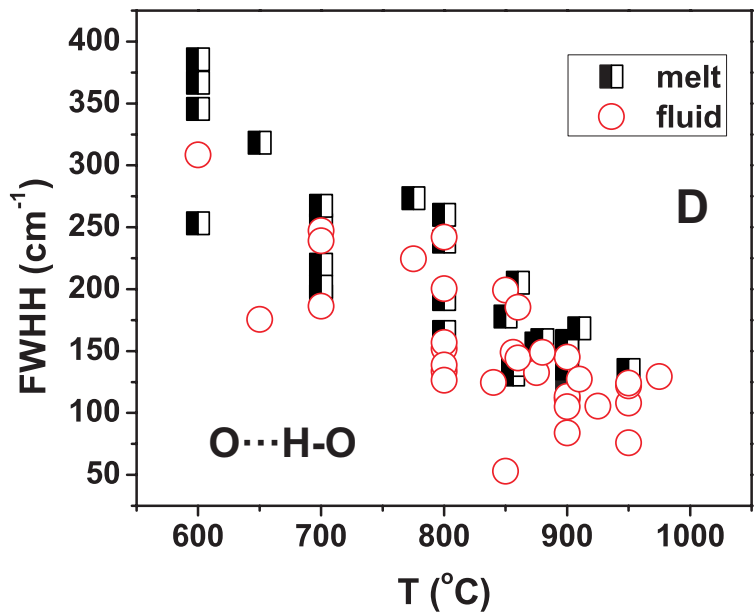
melt
fluid
D
O···H-O
FWHH (cm^{-1})
T (°C)

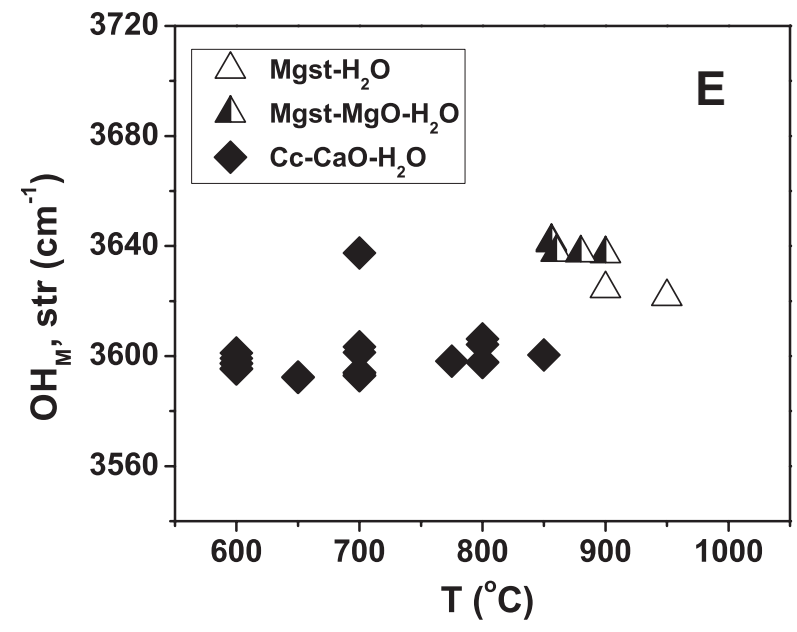
Mgst-H$_2$O
Mgst-MgO-H$_2$O
Cc-CaO-H$_2$O
E
OH$_M$, str (cm^{-1})
T (°C)

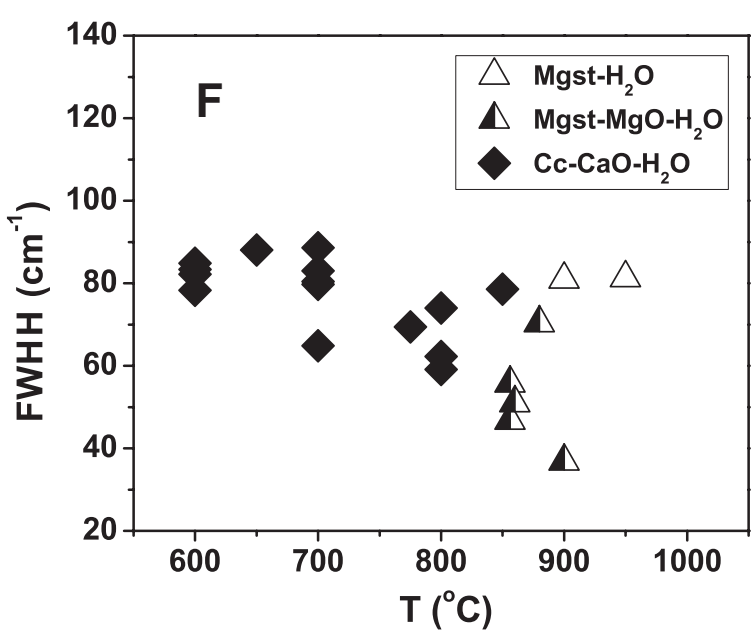
Mgst-H$_2$O
Mgst-MgO-H$_2$O
Cc-CaO-H$_2$O
F
FWHH (cm^{-1})
T (°C)

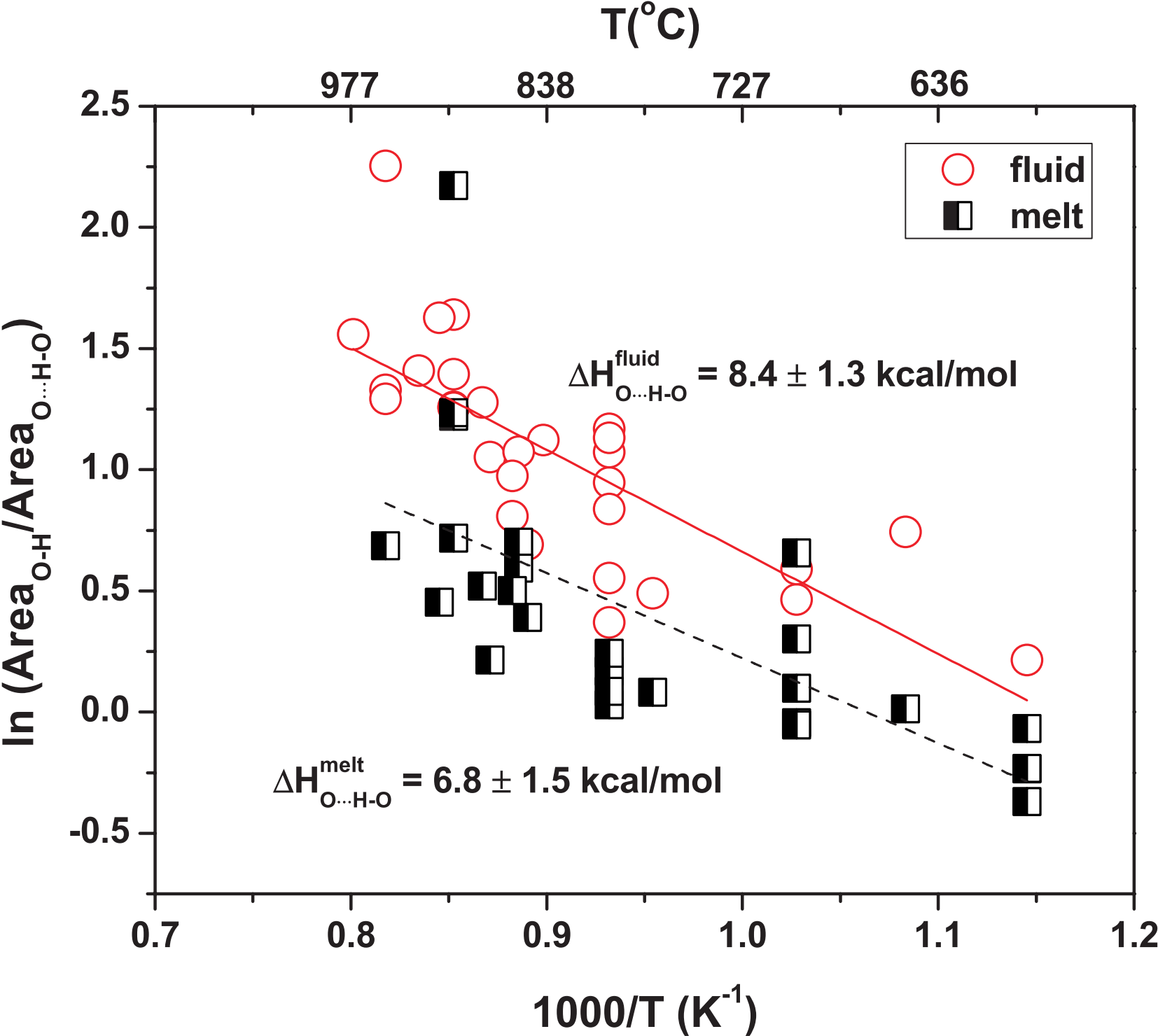
T(°C)
977
838
727
636
2.5
2.0
1.5
1.0
0.5
0.0
-0.5
ln (Area$_{O-H}$/Area$_{O\cdots H-O}$)
fluid
melt
$\Delta H^{fluid}_{O\cdots H-O}$ = 8.4 ± 1.3 kcal/mol
$\Delta H^{melt}_{O\cdots H-O}$ = 6.8 ± 1.5 kcal/mol
0.7
0.8
0.9
1.0
1.1
1.2
1000/T (K^{-1})

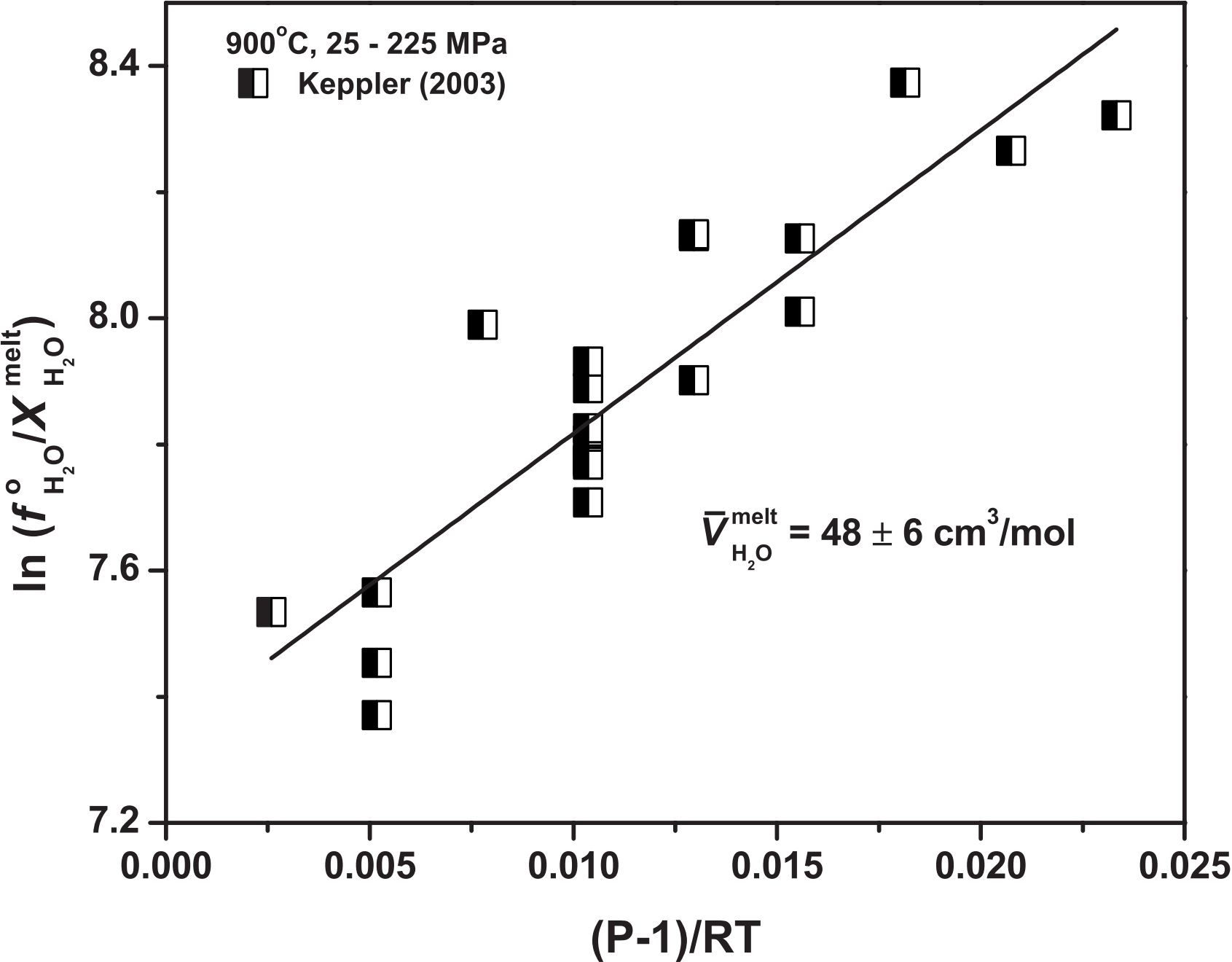
900°C, 25 - 225 MPa
Keppler (2003)
$\bar{V}^{melt}_{H_2O}$ = 48 ± 6 cm^3/mol
ln ($f^o_{H_2O}/X^{melt}_{H_2O}$)
(P-1)/RT
8.4
8.0
7.6
7.2
0.000
0.005
0.010
0.015
0.020
0.025